universität wien

MASTERARBEIT / MASTER'S THESIS

Titel der Masterarbeit / Title of the Master's Thesis

Towards optical cooling of silicon nanoparticles in a microcavity

verfasst von / submitted by

Franz Ferdinand Wieser, BSc

angestrebter akademischer Grad / in partial fulfilment of the requirements for the degree of

Master of Science (MSc)

Wien, 2017 / Vienna, 2017

Studienkennzahl lt. Studienblatt / degree programme code as it appears on the student record sheet:	A 066 876
Studienrichtung lt. Studienblatt / degree programme as it appears on the student record sheet:	Masterstudium Physik
Betreut von / Supervisor:	Univ.-Prof. Dr. Markus Arndt
Mitbetreut von / Co-Supervisor:	

Acknowledgments

I would like to express my deepest gratitude to my family, my colleagues and especially to my supervisor Prof. Markus Arndt who has opened up many opportunities for me that would have otherwise been out of reach. During the two years that I have spent in his group I have learnt valuable lessons on physics and research beyond the scope of an ordinary lecture. I am also indebted to Stefan and James who have taught me useful experimental methods and have considerably advanced my understanding of the interplay between theory and practice.

Abstract

Optomechanics is a rapidly advancing field with potential applications in many areas of research ranging from fundamental tests of physics and thermodynamics to sensing. Recently, technological advances in the fabrication of micro- and nanooptical systems have opened up new parameter regimes and hold great promise for future experiments. In particular, individual nanoparticles coupled to microcavities have emerged as a viable route towards the quantum regime on the mesoscopic and eventually even macroscopic scale. The size of the objects under investigation naturally makes them good candidates for tests of the superposition principle which is manifest in the interference of matter-waves. Cavity cooling is a way to slow down the motion of nanoparticles through their interaction with light and prepare them for interferometry. A novel set of open-access, high-finesse microcavities with small mode volumes for this purpose was characterized in a new experimental setup. Dispersive coupling of nanoparticles has been observed and paves the way for cavity cooling in the $10^6 - 10^9\ \mathrm{amu}$ mass range.

Contents

Introduction

The wave nature of all matter has challenged our physical intuition since it was first proposed by de Broglie in 1923 [1] and later observed with electrons [2], atoms [3], neutrons [4] and even molecules [5]. A conflict between theory and everyday experience arises as expressed by a well-known paradox due to Schrödinger [6] raising the question why quantum phenomena largely disappear in our familiar macroscopic environment. Although the principles of quantum mechanics are well founded experimentally on the microscopic scale the nature of the transition to the classical regime and the loss of coherence in increasingly macroscopic systems remains unclear. While superpositions of ensembles of ultracold atoms [7] and complex molecules [8] have already demonstrated quantum effects on previously inaccessible length and mass scales, respectively, non-linear extensions of unitary time evolution [9] and the effects of gravity [10–12] on a delocalized state are predicted to be observable around 10^6 to 10^{11} atomic mass units [13]. A matter-wave interferometer based on the diffraction of very massive particles naturally involves long interaction and coherence times, therefore it requires sources of slow particles. In particular, the momentum spread in the direction perpendicular to the plane of a diffraction grating with period d has to be smaller than the grating momentum h/d and the state should extend over several slits. Laser cooling in the sense of resonant scattering can drastically reduce the velocity of an atomic beam and achieve high phase-space densities [14, 15]. The minimum energy in Doppler cooling $\hbar\gamma/2$ is given by the linewidth γ of the atomic transition [16] but can be overcome by using more sophisticated methods

involving polarization gradients [17] or a coherent transfer between three energy levels [18]. These techniques together with evaporative cooling have enabled the wide field of ultracold quantum gases with far-reaching consequences for high-precision measurements [19], many-body physics [20] and quantum computation [21, 22]. While some of these methods have successfully been applied to small molecules such as strontium monofluoride [23] and strontium monohydroxide [24], composite objects such as polyatomic molecules or nanoparticles with a dense manifold of internal states can generally not be addressed by light in the same way. They no longer behave as an effective two-level system but dissipate energy to off-resonant states. Nonetheless, the prospect of high-resolution spectroscopy and fundamental tests of physics has motivated the development of new ways to reach lower temperatures in these systems. In particular, a large number of species and the existance of long-range dipole interactions make molecules an intriguing platform to study chemistry and physics in the ultracold regime. An indirect way of cooling is the assembly of weakly bound molecules from two atoms by photo- or magnetoassociation [25, 26]. Using stimulated Raman transitions they can be transferred into the vibrational ground state. While this method produces samples with high phase-space density it is restricted to a few possible combinations of alkaline and alkaline earth atoms. In contrast, sympathetic cooling in a buffer-gas relies only on elastic collisions at thermal equilibrium. Initially hot particles transfer a fraction of their kinetic energy to colder atoms, typically a noble gas at $2 - 10$ K, in every collision until they become thermalized inside an enclosed volume held at a constant temperature [27]. An effusive beam extracted through a small aperture of the cold cell has been used to load magneto-optical traps [28], resolve rotational spectra [29] and is being considered for the search of the electron's electric dipole moment [30]. Apart from the strong acceleration or deceleration in resonant interactions the

conservative forces exerted by light can also manipulate the motion of dielectric particles. Early experiments showed that trapping of polystyrene microspheres [31], viruses and bacteria [32] and even entire cells [33] through the dipole force is possible in a strongly focused laser beam. Parametric feedback of a levitated particle in such a dipole trap creates a time-dependent potential and effectively removes entropy from the system. Position and velocity are measured continuously to adjust the intensity, and therefore the stiffness of the trap, leading to mK temperatures at high-vacuum [34, 35]. Although the primary interest has so far been the center-of-mass motion, substantial effort is now also devoted to the study of rotational degrees of freedom [36–38]. Rotating nanoparticles have been proposed for sensing applications [39, 40] and the detection of short-range forces [41]. The ability to precisely control levitated nanorods [42] through polarization inside a dipole trap has also motivated research on rotational cooling [43], rotational diffusion and synchronization of rotors [44]. Furthermore, it adds more tools to study microscopic thermodynamics in a low-dissipation environment [45]. Both Doppler and parametric feedback cooling require active manipulation of the light source. In contrast, the conditions imposed on the light by an optical resonator enable a purely passive scheme. The idea behind cavity cooling is to replace the well-defined energy levels of an atom by the resonance of a high-finesse cavity [46, 47]. A dissipative interaction arises from the delayed reaction of the field to the optomechanical coupling, i.e. the cavity provides self-induced feedback cooling without the need to actively control the intensity of the light source. Alternatively, the process can be understood as a preferential photon scattering into the blue-shifted motional sideband transferring kinetic energy of the particle to the field. This idea has been demonstrated experimentally for single atoms [48], nanoparticles with a size on the order of $100\ \mathrm{nm}$ trapped at low-vacuum [49] and free-flying in high-vacuum [50] and charged nanospheres

inside an ion trap [51]. Even ground state cooling has been predicted for a variety of macroscopic objects such as cantilevers or membranes [52] and levitated objects in the absence of collisions with a background gas at ultra high-vacuum [49]. Levitated particles couple less strongly to the environment compared to clamped oscillators and once in the ground state of the trapping potential, a series of non-classical states of light may be mapped onto the center-of-mass motion [53, 54]. Cavity cooling has become part of an effort to create new and more realistic model systems of Schrödinger's cat through mechanical superpositions of massive objects. Unlike more conventional beam sources based on thermal evaporation or pulsed laser desorption, cavity cooling generally becomes more difficult as the size of the particles is getting smaller because the coupling strength decreases linearly with their volume. At the same time state-of-the-art matter-wave interferometers are currently not compatible with $10^{10}\ \mathrm{amu}$ silicon nanospheres for which cavity cooling has already been achieved. Talbot-Lau interference in the time domain using pulsed photo-depletion gratings [55] is currently limited to de Broglie wavelengths of $200\ \mathrm{fm}$ which corresponds to a still unattainable forward velocity of $0.2\ \mathrm{mm/s}$ for these particles. However, by using particles which are three orders of magnitude lighter in mass and have a velocity of $0.2\ \mathrm{m/s}$ the de Broglie wavelength already falls within the acceptance range. Furthermore, the existing setup can be stretched to permit even faster velocities. Likewise, a continuous long base-line molecule interferometer with $1\ \mathrm{m}$ separation between two gratings, i.e. a larger version of the Kapitza-Dirac-Talbot-Lau interferometer [56] can handle de Broglie wavelengths as small as $30\ \mathrm{fm}$. This research project is an attempt to bridge this gap with a new setup employing microfabricated mirrors. The stronger confinement of light as compared to conventional mirrors leads to an enhancement of the interaction and can take cavity cooling beyond its current limitations. Microcavities can provide

initially well-localized particles in the mass range of 10^6 to 10^9 amu, corresponding to $10 - 120$ nm diameter silicon spheres. High-finesse microcavities have only recently become available through advances in fabrication technology and were tested in a new setup designed and built to host future attempts to cool the motion of nanoparticles and eventually be attached to a suitable interferometer. The theory of light-matter interaction in a high-finesse cavity and how we use it for cooling will be discussed. First results on the characterization of these novel optical resonators are presented and evidence of 300 nm silica nanoparticles coupling to the cavity mode is shown. A new loading mechanism for slow, internally cold nanoparticles is then discussed together with an outlook on further steps.

Cavity cooling of nanoparticles

2.1 Optical cavities

An optical cavity is a set mirrors between which light is reflected repeatedly. The energy of the electromagnetic field is stored at multiple resonance frequencies and may even be coherently amplified by incorporating an active medium to produce a laser beam. Their frequency selectivity allows cavities to act as a spectral filter and some of the most advanced designs are used as references for ultrastable lasers [57]. At least three models of light are required to understand their behaviour. The geometric stability condition for the confinement of light is based on the description by rays [58]. We use wave optics to find the resonance frequencies and wavefunctions and eventually apply the photon picture to the interaction of dielectric objects with light inside the cavity. Now we consider two planar mirrors a distance d apart from each other. The electric field amplitude $u(\vec{r})$ is a solution of the wave equation

$$\left(\nabla^2 + k^2\right) u(\vec{r}) = 0 \tag{2.1}$$

where $k = 2\pi\nu/c$ is the wavevector vector. The boundary conditions that $u(\vec{r}) = 0$ at $z = \pm d/2$ permit only plane waves

$$u(\vec{r}) = u_0 \cdot \cos kz \tag{2.2}$$

with a frequency ν restricted to integer multiples of the free spectral range

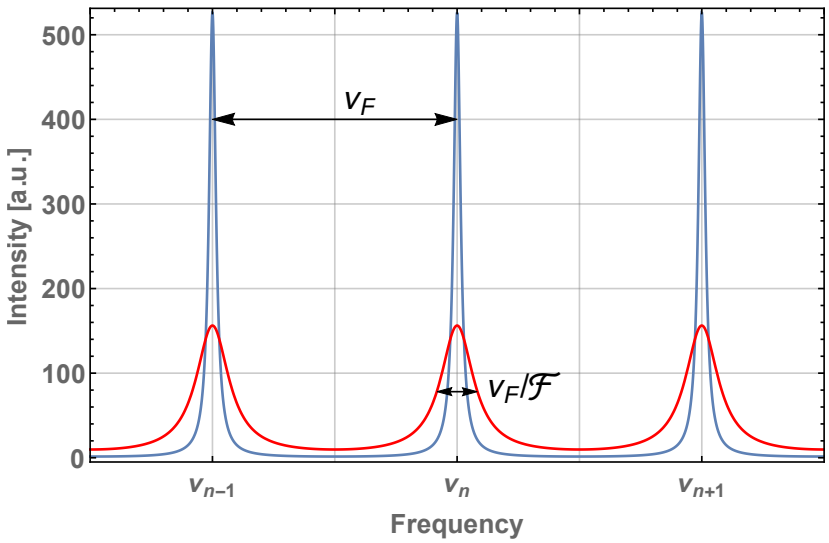

Figure 2.1: Transmitted intensity (2.4) through a low-finesse (red) and a high-finesse (blue) cavity. The higher the mirror reflectivity, and therefore the finesse, the more the spectrum ressembles a series of delta functions at integer multiples of the free spectral range.

$\nu_F = c/2d$, i.e. the resonance frequencies are uniformely spaced. Likewise, we may think of the modes as waves that reproduce themselves after one round-trip. The acquired phase shift of $\phi = 2kd$ has to be an integer multiple of 2π leading to the same resonance condition. In a realistic cavity the mirrors only have a finite reflectivity r and some light is lost in every round-trip. The electric field is the sum of all waves with equal relative phase. If the initial amplitude is u_0 then the total amplitude is

$$u = u_0 \sum_{n=0}^{\infty} r^n e^{-in\phi} = \frac{u_0}{1 - re^{-i\phi}} \tag{2.3}$$

The intensity $I = |u|^2$ is given by

$$I = \frac{I_0}{1 - \left(\frac{2\mathcal{F}}{\pi}\right)^2 \sin^2\left(\frac{\pi\nu}{\nu_F}\right)} \tag{2.4}$$

where $I_0 = |u_0|^2/(1-r)^2$ and $\mathcal{F} = \pi\sqrt{r}/(1-r)$ is the finesse providing a measure for the temporal confinement of light. It relates the free spectral range and the cavity linewidth κ through $\kappa = \nu_F/\mathcal{F}$.

2.2 Optomechanical interaction

Now we study the motion of a polarizable particle coupled to an electromagnetic field inside a cavity formed by two highly reflecting mirrors. Light is confined only at specific resonance frequencies ω_j which experience a position-dependent shift $g_0 = \partial\omega_j/\partial z$ in the presence of a dielectric object. This gives rise to a coupling of the nanomechanical motion and the time-dependent amplitude of the field which is the origin of the slowing force in cavity cooling. In order to find the equations of motion we assemble the complete Hamiltonian which contains terms describing the free field and an external drive, the free particle motion and the optomechanical interaction. First, we consider an empty cavity and quantize the electromagnetic field. In the classical picture it follows Maxwell's equations

$$\begin{aligned} \nabla \cdot \vec{B} &= 0 \\ \nabla \cdot \vec{E} &= 0 \\ \nabla \times \vec{B} &= \frac{1}{c^2}\partial_t \vec{E} \\ \nabla \times \vec{E} &= -\partial_t \vec{B} \end{aligned} \tag{2.5}$$

in the absence of charges and currents. However, the invariance of (2.5) under gauge transformations necessitates the choice of an additional constraint. Both the electric field $\vec{E} = -\partial_t \vec{A}$ and the magnetic field $\vec{B} = \nabla \times \vec{A}$ are determined by the vector potential $\vec{A}$ in the Coulomb gauge

$$\nabla \cdot \vec{A} = 0 \tag{2.6}$$

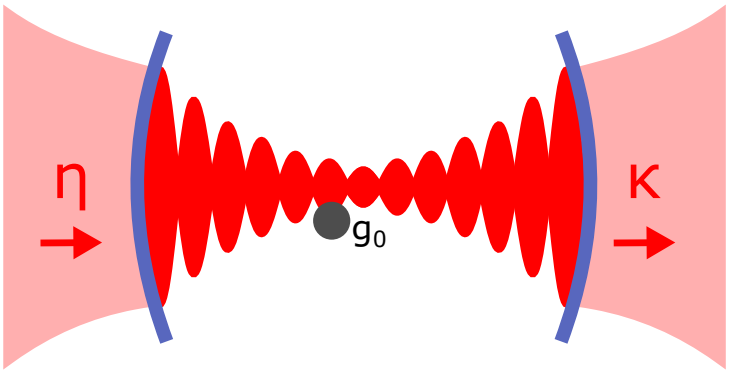

Figure 2.2: Cavity cooling of nanoparticles. A high-finesse cavity is driven by a strong laser field at a rate η and energy is dissipated at a rate κ through transmission, scattering or absorption in the mirror coatings defining the cavity linewidth. The interaction of a freely moving dielectric particle with the field is characterized by the optomechanical coupling strength g_0.

We substitute the definitions of $\vec{E}$ and $\vec{B}$ in terms of the vector potential into (2.5) and find that it is a solution of the wave equation

$$\left(\nabla^2 - \frac{1}{c^2}\partial_t^2\right)\vec{A}(\vec{r},t) = 0 \tag{2.7}$$

We analyze (2.7) in Fourier space and restrict the field to a single mode of frequency ω_0 and a finite volume V. The positive and negative frequency components of the vector potential $\vec{A}(\vec{r},t) = \vec{A}^{(+)}(\vec{r},t) + \vec{A}^{(-)}(\vec{r},t)$ then become

$$\begin{aligned}\vec{A}^{(+)}(\vec{r},t) &= \sqrt{\frac{\hbar}{2\omega_0\epsilon_0 V}}u(\vec{r})e^{i\omega_0 t}\alpha^* \\ \vec{A}^{(-)}(\vec{r},t) &= \vec{A}^*(\vec{r},t)^{(+)}\end{aligned} \tag{2.8}$$

where ϵ_0 is the dielectric constant and α is the amplitude of the field. The normalization ensures that α is dimensionless. The mode function $u(\vec{r})$ of the cavity fulfills the time-independent wave equation (2.1) and the apropriate boundary conditions imposed by the resonator geometry under consideration. The fundamental mode of a cavity with two spherical mirrors is a Gaussian beam whose

radius of curvature matches the mirror curvature at their position. More complicated spatial patterns such as Hermite-Gaussian or Laguerre-Gaussian beams emerge for higher order modes or different resonator geometries. Following the canonical quantization [59] we replace the amplitude in (2.8) by a non-hermitian annihilation operator a and impose the commutation relations

$$\begin{aligned} \left[a, a^\dagger\right] &= 1 \\ [a, a] = \left[a^\dagger, a^\dagger\right] &= 0 \end{aligned} \tag{2.9}$$

A mode of the cavity is then equivalent to a harmonic oscillator and the free Hamiltonian of the field with resonance frequency ω_0 becomes

$$H_0 = \hbar\omega_0 a^\dagger a \tag{2.10}$$

where $\langle a^\dagger a\rangle$ is the number of photons and the ground state energy is neglected. The interaction between the cavity mode and an external field at a laser frequency ω as well as the leaking of light due to the finite reflectivity of the mirrors are described by an exchange of photons of the form

$$H_1 \propto i\left(ba^\dagger - b^\dagger a\right) \tag{2.11}$$

While b annihilates a photon in the driving mode $a^\dagger$ instead creates one in the cavity mode. Due to time reversal symmetry and because the Hamiltonian must be a hermitian operator the opposite process is also possible. We assume a strong driving field with an amplitude η and negligible fluctuations around its mean such that (2.11) becomes

$$H_1 = i\hbar\eta\left(e^{-i\omega t}a^\dagger - e^{i\omega t}a\right) \tag{2.12}$$

Now we consider a dielectric particle interacting with the electric field which

is small compared to the wavelength. Therefore we can assume the field to be uniform across the extent of the particle and treat the interaction in first order dipole approximation. In general, this assumption is not always valid in the experimental situation. For larger particles the effective interaction averaged over the standing wave is smaller than for a point-like particle. A more rigorous treatment uses Mie scattering theory [60]. For a sub-wavelength particle the induced dipole moment is given by $\vec{d} = \chi \cdot \vec{E}$ where the polarizability χ of a homogeneously filled sphere increases linearly with volume. The energy of the dipole potential is given by

$$\begin{aligned} H_{\text{int}} &= -\chi \vec{E}^{(+)} \vec{E}^{(-)} \\ &= -\hbar g_0 |u(\vec{r})|^2 a^\dagger a \end{aligned} \tag{2.13}$$

where $g_0 \equiv \omega_0 \chi / 2\epsilon_0 V$ is the optomechanical coupling constant describing the change of the resonance frequency with respect to the particle position. The complete Hamiltonian for the coherent dynamics of the system in a reference frame rotating at the laser frequency becomes

$$H = -\hbar \Delta a^\dagger a + \frac{p^2}{2m} - \hbar g_0 |u(\vec{r})|^2 a^\dagger a + i\hbar\eta \left(a^\dagger - a\right) \tag{2.14}$$

where $\Delta = \omega - \omega_0$ is the detuning and p is the particle momentum. The first term describes the free cavity field, the second term represents the kinetic energy of the particle, the optomechanical interaction is contained in the third term and the last term describes the pumping of the cavity with a laser.

2.3 Momentum diffusion

Absorption, emission and scattering of cavity photons off the particle into free space induce a diffusion in momentum space and will cause both particle and light

field to evolve into a mixed state. The motional state and the field amplitude are then described by a density operator ρ which follows a master equation

$$\partial_t \rho = -\frac{i}{\hbar}[H, \rho] + \mathcal{L}\rho \tag{2.15}$$

where H is given by (2.14) and $\mathcal{L}$ is a linear superposition of operators describing each of these incoherent processes [60]. Absorption occurs at a rate proportional to the number of photons $\langle a^\dagger a \rangle$ and the imaginary part of the complex polarizability of the particle. It causes a momentum kick $\hbar\vec{k}$ at random times resulting in a diffusion along the cavity axis which becomes relevant only in the regime where the particle momentum $p \sim \hbar k$ is comparable to the photon momentum. The kinetic energy is then limited by the recoil due to a single photon. Since a nanoparticle has many internal degrees of freedom among which it can distribute additional energy from photon absorption, it heats up and may eventually even disintegrate. Furthermore, a particle with elevated internal temperature may emit thermal radiation leading to a similar diffusion effect. If the temperature T of the particle is well above the temperature of the environment the emission rate into a vacuum mode of frequency ω is given by a rate proportional to the Boltzmann factor. Once the particle is in thermal equilibrium with the environment the respective rate is given by Planck's law. Here, all experiments are performed in high-vacuum and the influence of residual gas on thermalization is negligible. Finally, elastic scattering of photons can be regarded as absorption from the cavity mode and subsequent emission into free space and therefore contributes to momentum diffusion. However, since the emission event occurs in a random direction it gives no contribution to the mean force. A sub-wavelength particle scatters light with the same angular distribution as a dipole and a rate proportional to the square of its volume. The non-isotropic character becomes important in the detection of the particle motion through the scattered light as

the intensity vanishes along the axis of polarization and is maximal in the perpendicular direction. The master equation (2.9) can be extended to n particles and m modes where a significant enhancement of damping is predicted as m increases [61].

2.4 Classical motion

In the experimental setup described below and previous demonstrations of cavity cooling [49, 50] the nanoparticles are well above the regime where the quantum nature of the light-matter interaction and the influence of momentum diffusion become significant. Therefore, we can describe the particle motion and the time evolution of the cavity field in a classical limit. The time evolution of the field amplitude is obtained by inserting the Hamiltonian (2.14) into (2.15) and additionally introducing a loss term $\mathcal{L} = -\kappa a$ to find

$$\partial_t a = -(i\Delta + \kappa)a + \eta - ig_0|u(\vec{r})|^2 a \tag{2.16}$$

where we have used the commutator relation $[a^\dagger a, a] = -a$. An identical rate equation can be formulated in a purely classical context and from now on we will disregard the quantum properties of a and simply treat it as a complex number. For an empty cavity (2.16) reduces to

$$\partial_t a = -(i\Delta + \kappa)a + \eta \tag{2.17}$$

and in the steady-state $\partial_t a = 0$ the amplitude is given by

$$\alpha_0 = \frac{\eta}{i\Delta + \kappa} \tag{2.18}$$

Now we consider a point-like nanoparticle interacting with the cavity field. We

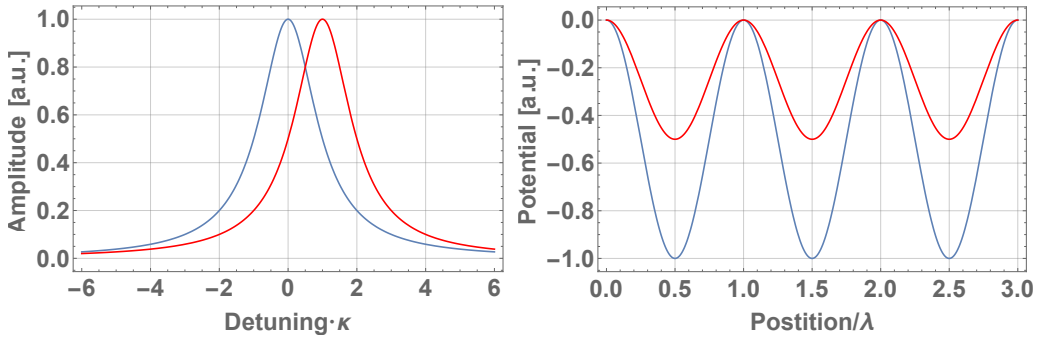

Figure 2.3: Dispersive coupling. An effective change of the cavity resonance frequency in the presence of a dielectric particle creates a time-dependent potential. The particle has to climb a potential hill which is always higher in the ascent than in the descent in a Sisyphus-like fashion.

neglect forces due to a radial intensity gradient and the motion along the direction of the standing wave is subject to a dipole force

$$m\partial_t^2 z = -\partial_z H_{\text{int}} \tag{2.19}$$

We separate the transverse spatial profile of the fundamental mode

$$|\tilde{u}(x,y)|^2 = e^{-2(x^2+y^2)/w_0^2} \tag{2.20}$$

where w_0 is the beam waist, from the standing wave $\cos kz$ along the z direction and (2.19) becomes

$$m\partial_t^2 z = -2\hbar k g_0 |\tilde{u}(x,y)|^2 |a|^2 \sin kz \cos kz \tag{2.21}$$

A dielectric particle interacting with the electromagnetic field changes the refractive index and thus the optical path length between the mirrors. Red-detuning the frequency of the laser from the cavity resonance leads to an intensity modulation which in turn induces a slowing of the motion along the cavity axis. The potential is strongest whenever the particle is in a bright region and weak-

est whenever it is in a dark region. The resulting time-dependent potential effectively removes entropy through a self-induced feedback [46, 47]. In order to determine the slowing force we consider (2.16) with a displaced amplitude $a+\alpha_0$ and assume $a \ll \alpha_0$, i.e. only small fluctuations around the steady-state. The formal solution is obtained by applying a variation of parameters with the initial condition $a(t) = 0$ for $t \to -\infty$ leading to

$$a(t) = -ig_0\alpha_0 \int_{-\infty}^{t} dt' e^{(i\Delta+\kappa)(t'-t)} |u(\vec{r})|^2 \tag{2.22}$$

For a plane wave $u(\vec{r}) = \cos(k(z + v(t' - t))$ subject to a time dependent Doppler shift which is propagating between two infinitely extended mirrors the integral is given by

$$a(t) = -\frac{g_0\alpha_0}{4}\left(\frac{2}{\Delta - i\kappa} + \frac{e^{i2kz}}{(\Delta + 2kv) - i\kappa} + \frac{e^{-i2kz}}{(\Delta - 2kv) - i\kappa}\right) \tag{2.23}$$

and the average force over one wavelength is

$$\overline{F(v)} = 2\hbar k \frac{g_0^2|\alpha_0|^2\kappa}{4}\left(\frac{1}{(\Delta - 2kv)^2 + \kappa^2} - \frac{1}{(\Delta + 2kv)^2 + \kappa^2}\right) \tag{2.24}$$

where kv is the Doppler frequency shift induced by the nanoparticle motion. For $|kv| \ll |\Delta|, \kappa$ the cavity field exerts a linear friction force with a damping coefficient

$$\gamma = \frac{4\hbar k^2 g_0^2 |\alpha_0|^2 \kappa \Delta}{(\Delta^2 + \kappa^2)^2} \tag{2.25}$$

and the kinetic energy approaches its limit $\hbar\kappa/2\sqrt{3}$ for a detuning of $\Delta = -\kappa/\sqrt{3}$ given by the balance with momentum diffusion. Improving the coupling constant g_0 in microcavities with a smaller mode volume increases the cooling

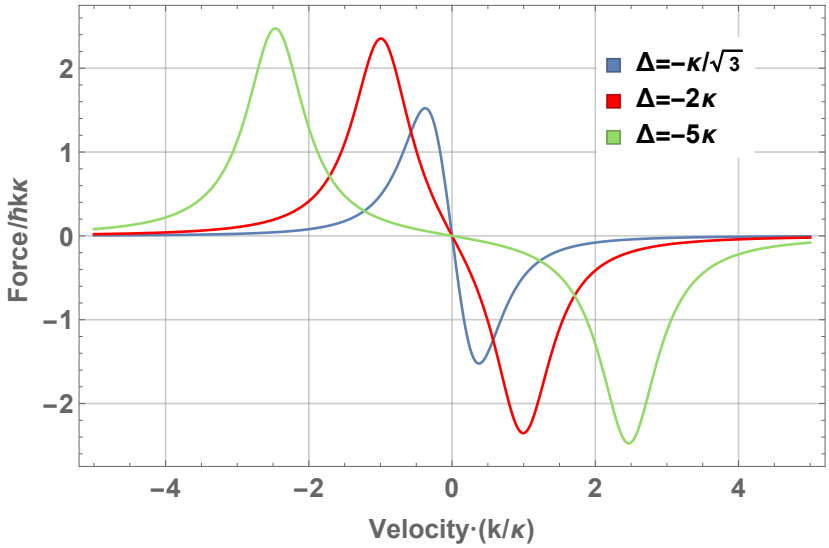

Figure 2.4: Slowing force for different settings of the detuning. Around $v = 0$ the force is linear and the respective cooling rate is given by (2.25) which is maximal for $\Delta = -\kappa/\sqrt{3}$. The range of velocities for cooling is given by $kv \simeq \Delta$ for large detunings.

rate. However, optical cooling in a single mode of the cavity is limited by residual conservative light forces. Once the velocity becomes very small the particle is trapped along an antinode with a potential strength $\hbar g_0 |\alpha_0|^2$. An increase of the intensity will inevitably reduce the range for cooling because the particles are trapped at higher velocities and only couple quadratically to the field. Reaching lower temperatures requires either longer interaction times or faster cooling rates. A superposition of two or even more adjacent cavity modes with appropriately chosen intensities and detunings can significantly enhance damping of the motion while cancelling the optical potential [62]. A generalization of (2.16) and (2.21) to multiple modes with different resonance frequencies and detunings is straightforward by applying the superposition principle to the individual forces. For two modes with detunings $\Delta_{1,2}$, steady-state amplitudes $|\alpha_{1,2}|$ and mode functions $u_{1,2}(\vec{r})$ they are given by

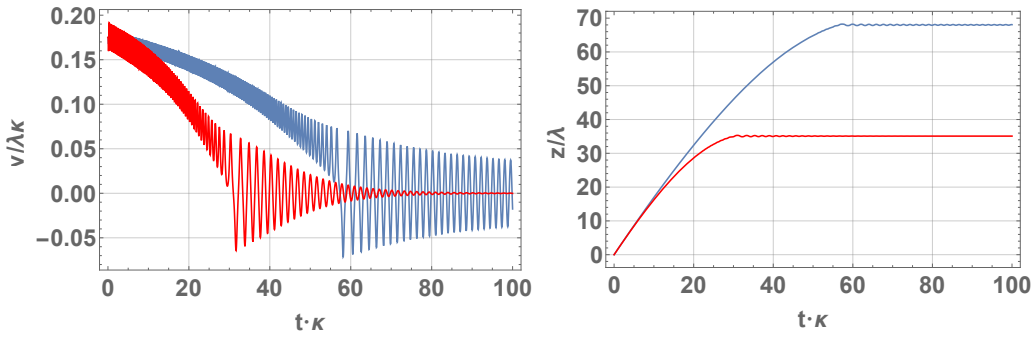

Figure 2.5: Two-mode cavity cooling. A significant enhancement of the cooling rate and lower temperatures as compared to a single mode (blue) are expected for two longitudinal modes (red). The particle velocity and position are obtained by solving (2.16) and (2.21) for a single mode and (2.26) for a two-mode setup.

$$\begin{aligned}
\partial_t a_1 &= -(i\Delta_1 + \kappa)a_1 - ig_0|u_1(\vec{r})|^2(a + \alpha_1) \\
\partial_t a_2 &= -(i\Delta_2 + \kappa)a_2 - ig_0|u_2(\vec{r})|^2(a + \alpha_2) \\
\partial_t^2 z &= -\frac{g_0^2}{m}\left(|\alpha_1|^2\partial_z|u_1(\vec{r})|^2 + |\alpha_2|^2\partial_z|u_2(\vec{r})|^2\right)
\end{aligned} \tag{2.26}$$

At equal and opposite detunings $\Delta_1 = -\Delta_2$ and equal drive strengths the motion is unaffected. In the case where $|\alpha_1| = |\alpha_2|$ the optical potentials cancel and the non-conservative forces accelerate the particle if $\Delta_{1,2} > 0$ or decrease the velocity if both modes are red-detuned. In Fig.2.5 two adjacent TEM_{00} modes of the cavity are driven at equal strengths and detuned by one linewidth.

Experiment

3.1 Microcavity array

An array of 10×10 micromirrors was fabricated by G. Wachter and M. Trupke at the University of Vienna into a single-crystal silicon wafer by a two-step etching procedure and a surface roughness below 1 nm is obtained by repeated smoothing. For this purpose a $2 \ \mu\text{m}$ silicon dioxide layer is grown by oxidation and removed by hydrogen fluoride. The structures are evenly distributed with a spacing of $500 \ \mu\text{m}$ along both directions. The radii of curvature range from $100 \ \mu\text{m}$ to 1.3 mm and are up to two orders of magnitude smaller than for mirrors on conventional glass substrates. A dielectric coating for the operating

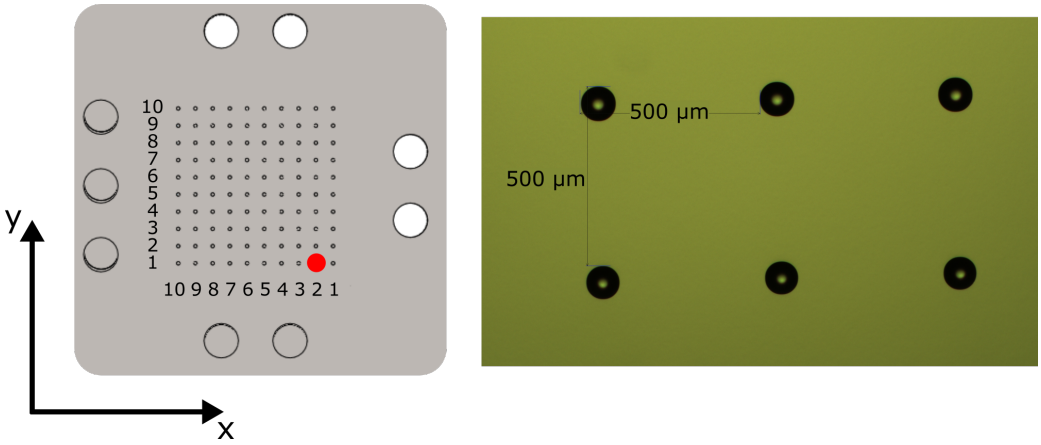

Figure 3.1: *Left*: Schematic view of the silicon chip with numbering and coordinate system used for characterization. In our notation, the second mirror to the right in the bottom row (red dot) is labeled $(1, 2)$. Higher numbers indicate a smaller radius of curvature. *Right*: Image of microfabricated mirrors taken with an optical microscope.

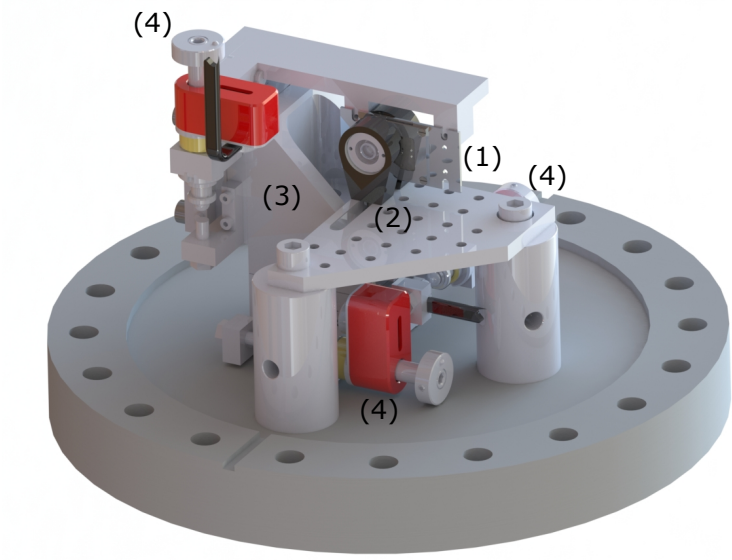

Figure 3.2: Vacuum setup with microcavities. (1) The chip is inserted into an aluminum frame and mounted onto an adapter. (2) An aspheric lens is used to couple light into the cavities. An identical lens is positioned behind the chip to collect the transmitted light. (3) The chip is aligned by a set of translation stages clamped onto the bottom vacuum flange. (4) Picomotors with a resolution $< 30\ \mathrm{nm}$ actuate the stages.

wavelength of $1550\ \mathrm{nm}$ with a target transmission of $15\ \mathrm{ppm}$ is applied to the front side as well as an anti-reflex coating on the back side. Openly accessible cavities are formed from two matching chips and aligned using a $105\ \mu\mathrm{m}$ silicon spacer. After assembling the parts under a microscope they are mechanically clamped and inserted into an aluminum frame.

3.2 Vacuum

In principle, cavity cooling can be performed even under ambient conditions but for consistency with future applications and since the damping effect and the final temperature depend on the background pressure this experiment is conducted in a high-vacuum environment. The vacuum setup consists of an electropolished

chamber with an additional pumping region connecting a vibrationally isolated turbo molecular pump. After baking at $120\ ^{\circ}\mathrm{C}$ for 8 hours we reach a pressure of $2{\cdot}10^{-8}\ \mathrm{mbar}$ in the empty chamber. While the experiment is running the pressure is typically an order of magnitude higher. The bottom flange was equipped with threads for mounting a 3D translation stage and a custom breadboard for two lenses. Every linear stage is positioned with better than $30\ \mathrm{nm}$ resolution by a piezoelectric actuator. The chip is mounted onto a custom adapter. Since samples have to be exchanged frequently the chamber is vented with dry nitrogen to reduce contamination by adsorption of condensable content in ambient air and to ensure faster pumping.

3.3 Nanoparticle desorption

A difficult step in any experiment involving a non-volatile sample is to controllably introduce particles into the gas phase. Cavity cooling places additional constraints on the initial velocity distribution because it requires sufficiently long interactions times. Laser-induced thermomechanical stress (LITHMOS) has proven successful in launching nanoparticles into high-vacuum with $v \leq 1\ \mathrm{m/s}$ in the forward direction [50]. A strong ns laser pulse is applied to a pure silicon wafer or a substrate with nanofabricated structures [63]. While the release of spheres from cracks in the surface of plain silicon is a probabilistic process, nanofabricated samples are more reproducable and can have a predefined shape. A particularly interesting object are silicon nanorods because their anisotropy leads to enhanced coupling at a given mass [43] and introduces additional degrees of freedom [63]. A similar method of desorption uses laser pulses to induce acoustic shock waves in a metal foil coated with a thin sample layer [64]. They break the surface bonds and release the particles into free flight. For testing

purposes we prepare readily available $300\ \mathrm{nm}$ silica spheres by dissolving them in acetone, sonicating them for $60\ \mathrm{min}$ and applying a few drops of solution onto an aluminum foil. We use a frequency-doubled Nd:YAG laser with a wavelength of $532\ \mathrm{nm}$, pulse lengths of $10\ \mathrm{ns}$ and pulse energies of $1 - 10\ \mathrm{mJ}$ for desorption. The beam is shared between three different experiments and directed by a combination of a half-wave plate and a beamsplitter and a removable mirror on a magnetically coupled base plate. A single lens focuses the pulses onto the back of the sample. The foil is positioned with a magnetic mount from the outside of the vacuum window. Since the window allows for multiple samples to be in place at once we rarely have to vent the chamber.

3.4 Optics

The laser system for driving the microcavities consists of a continuously tunable diode laser (Toptica CTL 1550) with a wavelength of $1550\ \mathrm{nm}$, an output power of $50\ \mathrm{mW}$ and a short term ($5\ \mu\mathrm{s}$) linewidth below $10\ \mathrm{kHz}$ and mostly fiber-based optical elements. Silicon has both a high polarizability and low absorption at this wavelength. The optical properties provide a 2.7-fold increase in dispersive coupling g_0 over SiO_2 while also avoiding strong heating or even thermal decomposition in the cavity field. Furthermore, optical fibers show minimal attenuation at the chosen telecom wavelength. The laser light is coupled into a single mode fiber with approximately $50\ \%$ efficiency and can be passed through an electro-optic modulator with a bandwidth of $12\ \mathrm{GHz}$ for characterization measurements. We connect polarization controlling pedals which allow an adjustment of the incoming polarization by applying mechanical stress to the fiber. The beam is aligned using a mirror outside the vacuum chamber and the translation stages. Focusing onto the cavities and collimation of the transmit-

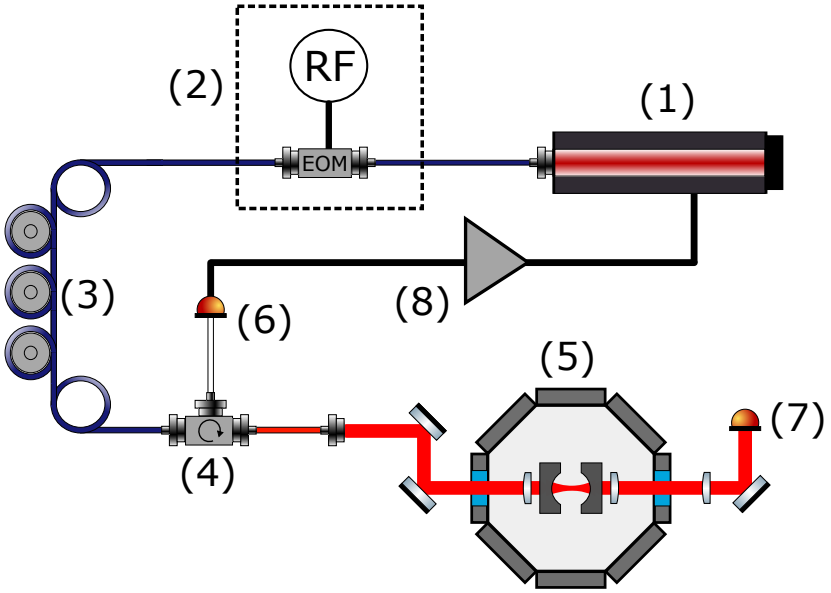

Figure 3.3: Optical setup for cavity cooling. (1) Tunable diode laser. (2) Electro-optical modulator (EOM) with RF drive for linewidth measurement. (3) Polarization controlling pedals. (4) Circulator. (5) Vacuum chamber with two aspheric lenses and microcavities. (6) Photodetector for reflected light. (7) Photodetector for transmitted light. (8) Electronic locking circuit.

ted light is achieved by identical $3\ \mathrm{mm}$ aspheric lenses. Both lenses have to be brought close to the chip because of the high refractive index of silicon and the shape of the cavity mode. A circulator redirects the reflected light onto a photo-detector and simultaneously acts as an optical isolator to prevent optical feedback to the laser. The transmission signal is read out on a fast oscilloscope where acquisition is triggered by the desorption pulse.

3.4.1 Laser locking

The cavity has a fixed length but is still subject to small drifts due to thermal and acoustic noise. In order to lock the laser frequency to the cavity its deviation from resonance has to be determined fast and with high signal-to-noise ratio, e.g. using the slope of the transmission peak or external frequency modulation.

The frequency difference is then converted into a voltage for electronic feedback by an integrator. The bandwidth of the locking circuit is fundamentally limited by the finite reaction time of the cavity, i.e. the cavity linewidth κ and fast fluctuations remain unaffected. Hence the modulation due to nanoparticles crossing the cavity, which is on the order of a few MHz, can still be detected because the locking circuit has a negligible response in this frequency range. This is also a prerequisite for cooling. Since frequency fluctuations are converted into amplitude fluctuations the feedback loop is not able to distinguish between a modulation of either one of them. We use the fluctuations of the reflected intensity along the side of the fringe as an error signal for feedback to the laser current. We apply additional feedback to the piezo controlling the offset of the center wavelength to achieve a greater locking range and counteract slow drifts on a timescale of several minutes.

3.4.2 Scattered light detection

We have detected nanoparticles inside the cavity mode through a modulation of the transmission signal. However, more precise information in real-time can be obtained from the scattered light [65]. Measuring both signals allows to determine the particle position and eliminate laser noise and the influence of electronic feedback. The intensity of the scattered light depends on the mode function of the spherical resonator

$$|u(\vec{r})|^2 = \cos^2 kz \cdot e^{-\frac{2(x^2+y^2)}{w_0^2}} \tag{3.1}$$

where w_0 is the waist and $k = 2\pi/\lambda$. We assume the particles are confined to the xz plane. The scattered light then shows two characteristic time scales. The width τ of the envelope corresponds to the forward velocity $v_x = w_0/\tau$ which

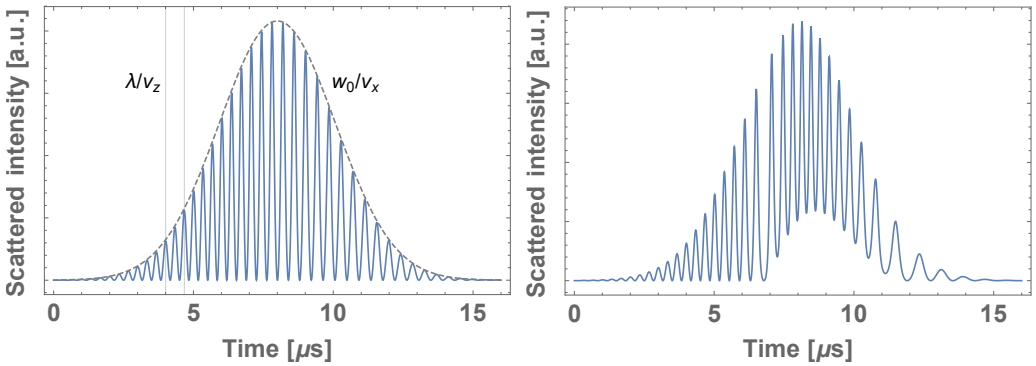

Figure 3.4: Simulated scattered light of a nanoparticle inside a high-finesse cavity. The time-dependent intensity reveals information about the velocities in both forward and transverse direction. The images are computed by solving (2.16) and (2.21) using the mode function (3.1). *Left*: We assume a cavity with a waist of $10\ \mu\mathrm{m}$, a detuning of $\Delta = -\kappa$, a pumping rate $\eta = 2 \cdot 10^3\kappa$, a coupling strength $g_0 = -0.1\kappa$ and an initial transverse velocity $v_z = 2\pi\kappa/\lambda$ where $\lambda = 1550\ \mathrm{nm}$. *Right*: At $2g_0$ the signal exhibits signs of trapping and cooling. In this case the scattered intensity is not dropping to zero around the center of the mode and shows a clear asymmetry, i.e. a bigger separation of maxima towards the right.

remains unchanged. The higher frequency is related to the transverse motion and the respective velocity v_z is determined from the separation between two local maxima or minima. Signitures of 1D trapping along an antinode of the field can be identified as well as rotational motion of non-spherical nanoparticles [63]. An approved method from previous experiments is adopted [65]. A multimode optical fiber is positioned by three linear translation stages and the collected light is focused onto a photodetector by a lens formed from a drop of fiber epoxy.

Results

4.1 Microcavity characterization

4.1.1 Picomotor calibration

In a first step the displacement of the microcavity chip by the linear translation stages in the transverse direction was calibrated using a $1392\ \mathrm{nm}$ laser diode. A lower finesse at this wavelength facilitates the coupling of light into the cavities. We measure the reflected and transmitted intensity on two photo-detectors to find the mirrors. They are identified as a local maximum of the reflected light. In order to calibrate the picomotors and the alignment of the chip with respect to the translation stage we record the number of steps between the center of two features in each row. Assuming the mirrors are separated by $500\ \mu\mathrm{m}$ we find that every step of the piezo actuator corresponds to $(23 \pm 1)\ \mathrm{nm}$ in the $+x$ direction and $(24 \pm 1)\ \mathrm{nm}$ in the $-x$ direction. We find that moving from one mirror to the next also requires a small adjustment of the vertical position. The rotation of the chip in the plane perpendicular to the optical axis was estimated by summing the number of steps in the vertical direction in each row. The average over the entire array gives a rotation by approximately $13\ \mathrm{mrad}$.

4.1.2 Finesse

We characterized a few cavities in the array using the $1550\ \mathrm{nm}$ tunable diode laser. We scan the laser frequency to find the resonance and determine the free

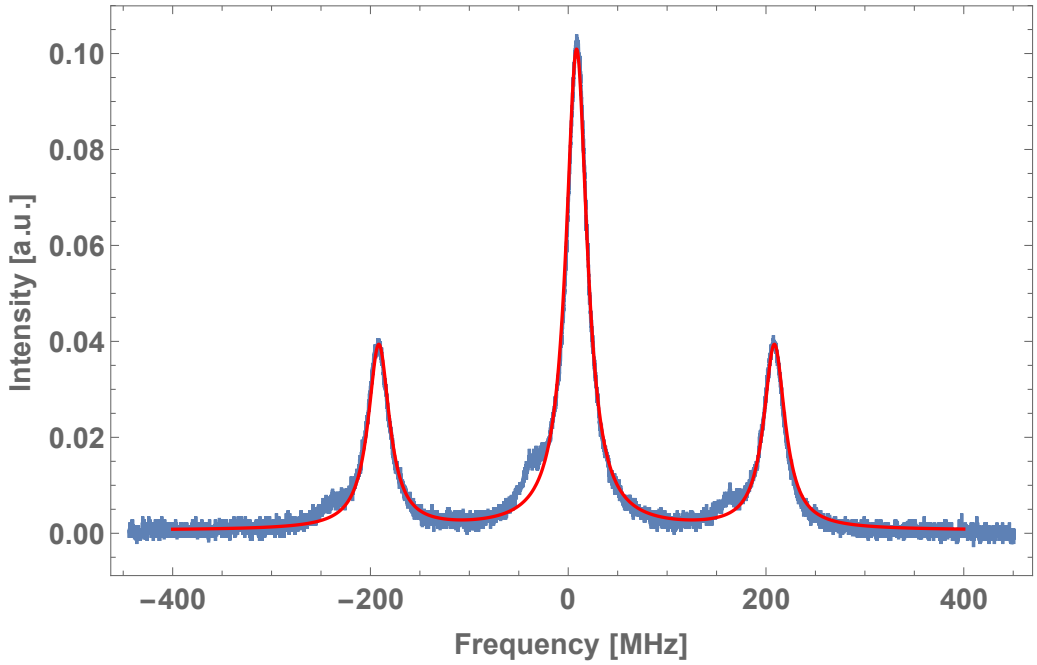

Figure 4.1: Measurement of the cavity linewidth κ of $(1,2)$ using 200 MHz sidebands and a non-linear fit. We average over a sequence of 100 frequency scans and obtain the finesse from its definition $\mathcal{F} = \nu_F/\kappa$.

spectral range. In order to measure the finesse of the microcavities we connect the electro-optical modulator and introduce symmetric sidebands to calibrate the frequency scan. The linewidth is extracted from a non-linear fit of the transmitted intensity as a function of the laser frequency with a sum of three Lorentzian functions

$$L(\nu) = \frac{I_0}{1+\frac{4F^2}{\pi^2}(\nu-\nu_0)^2} + \frac{I_1}{1+\frac{4F^2}{\pi^2}(\nu+(\nu_0-\nu_1))^2} + \frac{I_1}{1+\frac{4F^2}{\pi^2}(\nu-(\nu_0-\nu_1))^2} + A \tag{4.1}$$

where we make use of symmetry and average over 100 consecutive measurements for each cavity. In order to exclude systematic errors and drifts during the acquisition we compare the data histogram to a Gaussian distribution and look for trends in the measurement sequence. First, we carried out the above

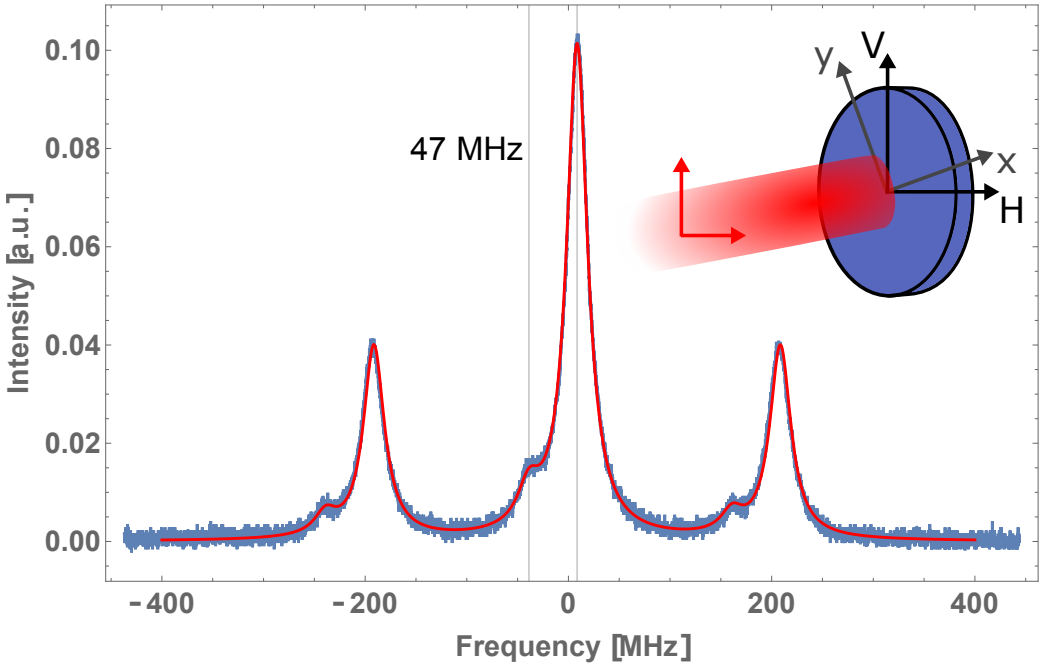

Figure 4.2: Birefringence of the micromirrors. The horizontal (H) and vertical (V) polarization of the incoming light are rotated with respect to the fast (x) and slow (y) axis which have indicies of refraction n_x and n_y, respectively. For $(1, 2)$ we observe a splitting of 47 MHz between the resonance frequencies of the two polarization modes.

procedure for the chip with a 105 μm full-frame spacer. The free spectral range for this case $\nu_F = (1.25 \pm 0.02)$ THz was measured on $(1, 2)$ resulting in a total cavity length of (120 ± 2) μm including the depth of the mirrors. We obtain a finesse of (47.000 ± 1000) in accordance with previous measurements of the same chip in a different setup. The data in Fig.4.1 exhibit residual birefringence which is suppressed for the measurement of the finesse by a applying the right wave-plate rotation with the polarization controlling pedals. Another fit with a sum of six Lorentzian functions gives a frequency splitting of 47 MHz between the two polarization components. The origin of birefringence may be a lateral misalignement of the laser beam, an imperfect mirror shape or anisotropic stress in the dielectric coating that occurs during the deposition process or the assembly

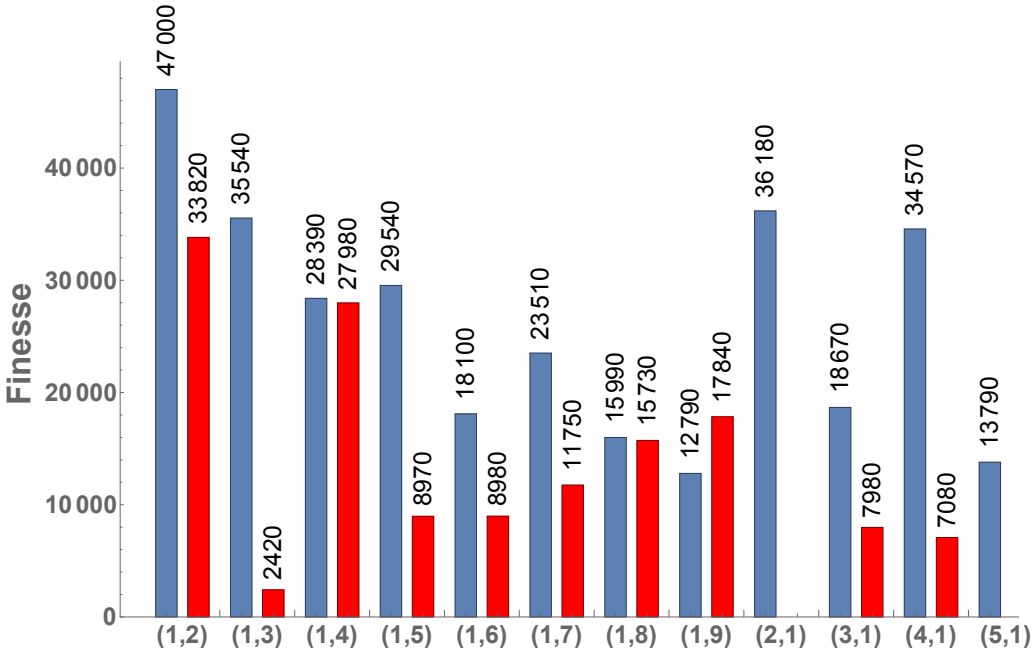

Figure 4.3: Comparison of cavity finesse with different spacers. We observe a significant difference between the assembly with a full-frame spacer (blue) and the open-access spacer (red). For $(2,1)$ and $(5,1)$ no resonance was found in the latter case. Hence the finesse seems to depend critically on the cavity length and the alignment of the chip.

of the cavities. This effect has to be considered in polarization sensitive experiments such as when working with non-spherical objects or in cavity quantum electrodynamics studies [66]. However, it has also been used for cavity stabilization [67]. Next, we repeated the measurement using an open-access $105\ \mu\mathrm{m}$ spacer on the same chip. We now find a free spectral range of $(1.15 \pm 0.02)\ \mathrm{THz}$ on $(1,2)$ resulting in a cavity length of $(130 \pm 3)\ \mu\mathrm{m}$. The finesse assumes lower values across the array. While the finesse is fundamentally limited by the reflectivity of the mirrors, it is determined in practise by non-parallel alignement or imperfections of the radius of curvature. For our purposes we require a high ratio of finesse and mode volume to maximize the coupling strength $g_0 \propto 1/V$ and hence the cooling rate. However, access to the cavity for introducing particles,

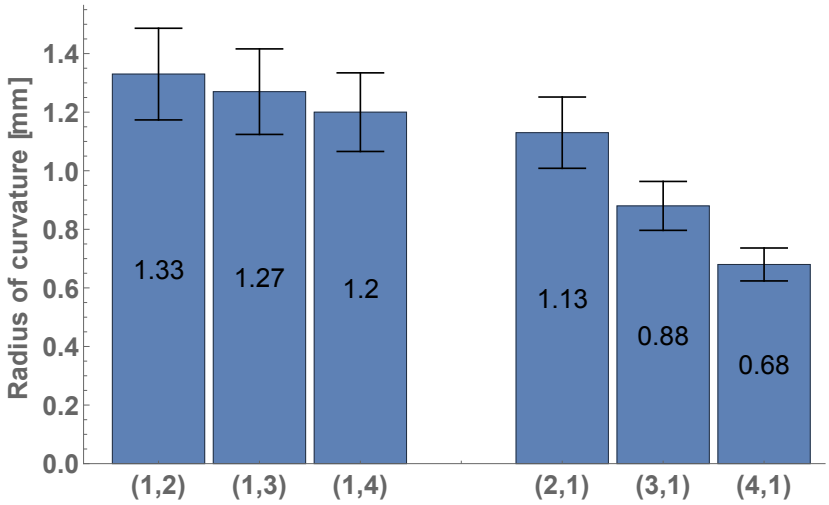

Figure 4.4: Radii of curvature for three neighbouring mirrors along a row and a column. By design they decrease faster along the column. Measurements were performed with a full-frame spacer and error bars represent standard deviation assuming Gaussian error propagation.

the fabrication of spacers and the radius of curvature put a constraint on the minimum cavity length.

4.1.3 Radius of curvature

While the finesse describes the temporal confinement of light, the second figure of merit for a microcavity is the mode volume which is a measure for the spatial confinement. It is given in terms of the cavity length $d = c/2\nu_F$ and the waist w_0 as $V_c = \pi w_0^2 d/4$. The waist of the Gaussian mode of a symmetrical resonator with identical concave mirrors is related to d and the radius of curvature R by

$$w_0^2 = \frac{\lambda d}{2\pi}\sqrt{\left(\frac{2|R|}{d} - 1\right)} \tag{4.2}$$

Each mirror in the array is fabricated with a different radius of curvature which

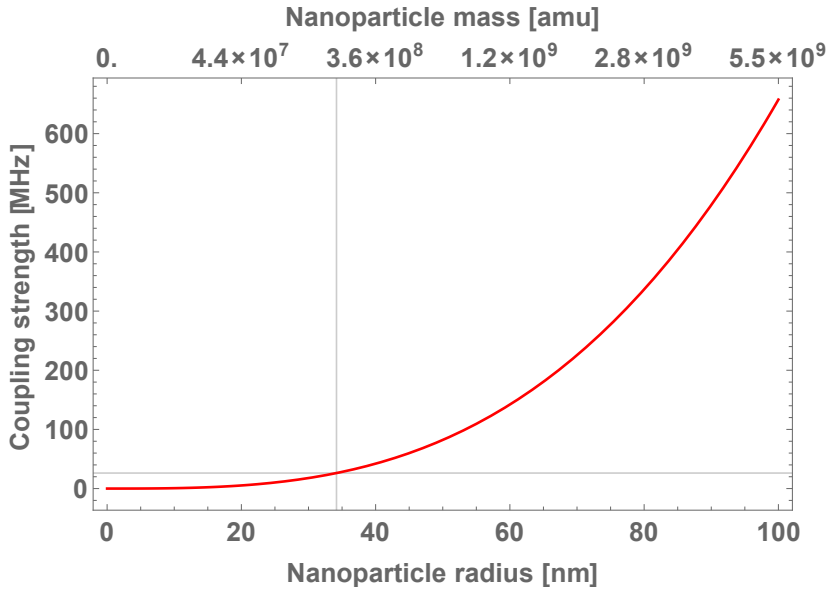

Figure 4.5: Coupling strength g_0 as a function of particle radius. For the cavity with a finesse of 47.000 strong coupling $g_0 \geq \kappa$ is achieved beyond $R_c = 34$ nm. The horizontal line marks the linewidth and the vertical line the critical radius.

is related to the frequency spacing $\Delta\nu$ of the fundamental TEM_{00} mode and the first-order transverse mode by

$$|R| = \frac{d}{1 - \cos\left(\frac{\pi\Delta\nu}{\nu_F}\right)} \tag{4.3}$$

We measure $\Delta\nu = (165 \pm 13)$ GHz for the cavity with the highest finesse and a full-frame spacer and obtain a radius of curvature $R = (1.33 \pm 0.16)$ mm corresponding to a beam waist of $w_0 = (12.0 \pm 0.5)$ μm at the center of the cavity. The measurements indicate the desired fast decrease in radius of curvature along a column and a slower decrease along a row of the chip. The Sisyphus-like cooling through the intensity modulation is most pronounced in the strong coupling regime $g_0 \geq \kappa$ [46]. For the maximum finesse cavity on the chip this condition is fulfilled for silicon nanospheres with a radius above 34 nm corresponding to a mass of $2 \cdot 10^8$ amu.

4.2 Detection of nanoparticles

Following the characterization of the setup we have introduced $300\ \mathrm{nm}$ silica spheres by laser desorption. The diode laser is red-detuned by $30\ \mathrm{MHz}$ to about 55% of the intensity maximum and locked onto the side of the fringe. The presence of a particle is manifest in the modulation of the transmission and reflection as it shifts the resonance frequency. While the envelope of the signal is also visible in the scattered light the fast dynamics have so far remained obscure due to an insufficient detector bandwidth. We even observe a shift exceeding the linewidth resulting in the appearance of truncated peaks. In order to extract the forward velocity the signal is low-pass filtered and the remaining envelope is fitted with a Gaussian function. The transverse velocity is determined from the separation of the peaks as the particle crosses the nodes and antinodes of the standing wave. For the nanoparticle shown in Fig. 4.6 we find $v_x = 11.4\ \mathrm{m/s}$ and $v_z = 5.9\ \mathrm{m/s}$. The aspect ratio $v_z/v_x \simeq 0.5$ is well outside the range permitted by the distance from the sample to the cavity and the aperture of the chip. The geometry of the experiment allows for particles with $v_z/v_x < 2.5 \cdot 10^{-3}$ to reach the cavity mode on a straight trajectory. For $v_x = 11.4\ \mathrm{m/s}$ the transverse velocity would be limited to $v_{z,max} = 2.8\ \mathrm{cm/s}$. Furthermore, the distance from the sample to cavity as calculated from the forward velocity and the time between the desorption laser pulse and the appearance of the particle in the transmission signal is shorter than the actual value. Therefore, the data suggest that deflection from the surface occurs inside the chip. We have reproduced the experimental results with a different sample. Transmitted and reflected light are shown in Fig. 4.7 for a nanoparticle with a forward velocity of $v_x = 10.3\ \mathrm{m/s}$ and $v_z = 4.3\ \mathrm{m/s}$. In both cases the particles are moving too fast across the standing wave for cooling to occur.

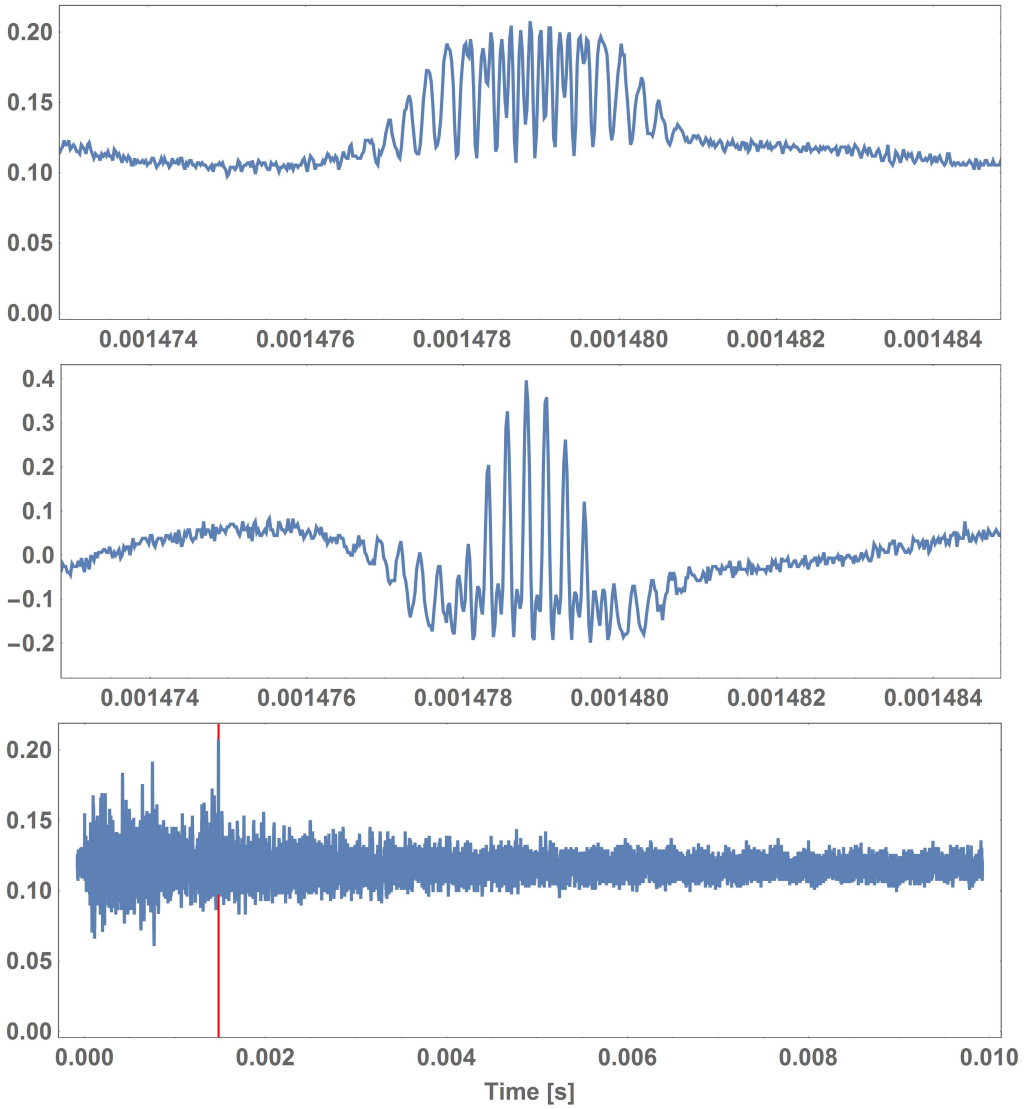

Figure 4.6: Nanoparticle detected in transmitted and reflected light. *Top*: Cavity transmission with modulation due to dispersive coupling. Towards the center of the mode the particle shifts the frequency over the resonance. *Middle*: Intensity of the reflected light. *Bottom*: The entire trace over an integration time of $10\ \mathrm{ms}$ triggered by the desorption laser pulse. A red line marks the appearance of the particle.

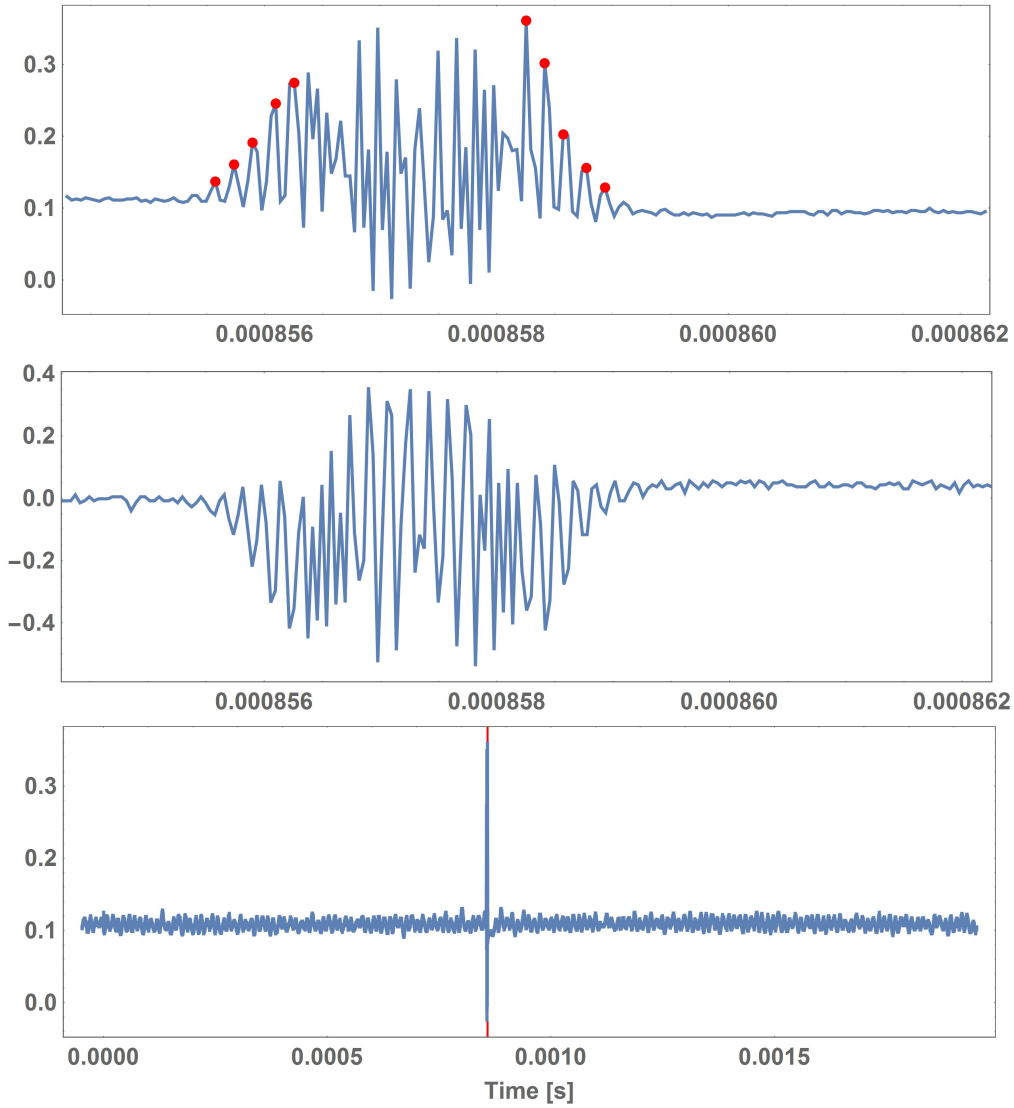

Figure 4.7: Another nanoparticle from a different sample with shorter acquisition time. The red points mark the detected peaks of transmission as the particle comes close to an antinode. Only the first 5 and last 5 data points were used in evaluating the transverse velocity.

Outlook

5.1 Cryogenic nanoparticle source

A major challenge in levitated optomechanics and cavity cooling is the availability of a source of slow nanoparticles. A longer interaction time with the mode results in a lower final temperature and advanced methods such as two-mode cooling become applicable. In pulsed laser desorption strong surface binding forces must be overcome and a substantial amount of energy is deposited into the sample within a short time. This inevitably leads to high kinetic energies and possibly raises the internal temperature of the ejected matter. A variation of this method employs a cryogenic matrix where particles are captured, thermalize and are eventually evaporated along with the buffer-gas. A similar source has previously been developed for mass spectrometry [68] and spectroscopy of lithium [69]. We create the matrix in situ by condensation of a buffer-gas on a cold surface. Deposition continues until the pressure of the gas p is equal to the saturation vapor pressure at the temperature of the surface. The surface temperature T_S rises as the layer thickness $x(t)$ increases until the system reaches equilibrium. We can describe the process by [70]

$$\begin{aligned} \rho\dot{x}(t) &= \alpha\phi - \phi_e \\ k\frac{dT_S(t)}{dx} &= \rho \cdot \Delta h \cdot \dot{x}(t) + \alpha\phi c_p(T_0 - T_S(t)) \end{aligned} \tag{5.1}$$

where α is the probability of condensation and T_0 is the initial buffer-gas tem-

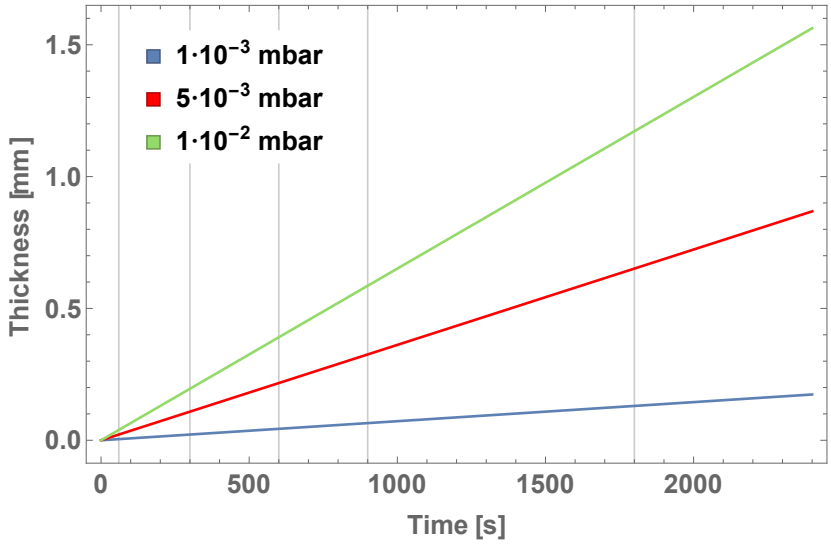

Figure 5.1: Layer thickness of argon on a $10\ \mathrm{K}$ surface as a function of time at different pressures in the free molecular regime. A capture coefficient of $\alpha = 0.8$ is used in (5.1).

perature. The mass transfer is given by the difference between the incident flux ϕ and the rate of evaporation ϕ_e whereas the surface temperature of the condensate changes through latent heat, sensible heat and conduction. The thermal conductivity k, the density ρ and the specific heat capacity c_p assume their values at T_0 and we consider a free molecular flow

$$\phi = \frac{p}{\sqrt{2\pi R T_0}} \tag{5.2}$$

where R is the universal gas constant. At $10\ \mathrm{K}$ thermal evaporation is negligible and we obtain an estimate for the layer thickness at various background pressures by inserting (5.2) in (5.1). At higher flow rates the buffer-gas is in the continuum regime and deposition rates can be significantly higher [70]. However, the influence of collisions and temperature gradients resulting from sudden freezing would require more involved considerations to estimate the layer thickness. In a separate vacuum system a preliminary setup was tested. A copper block is con-

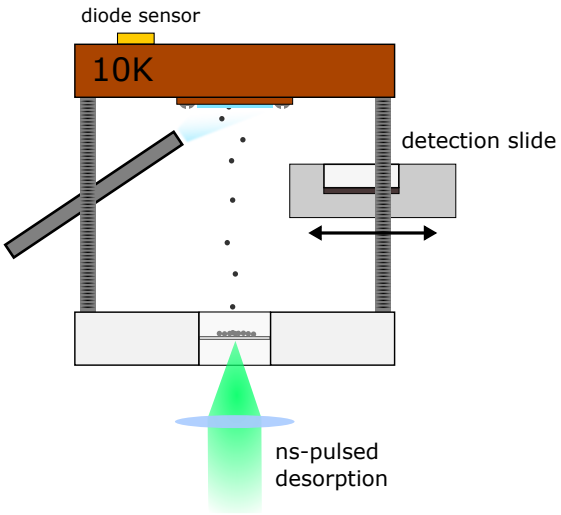

Figure 5.2: Cryogenic nanoparticle source. A solid argon matrix is created in situ on a copper foil. Silica nanoparticles are dropped onto a thin aluminum foil from an acetone solution and launched into high-vacuum by pulsed laser desorption. After implantation the detection slide is inserted below to capture them as the matrix evaporates.

nected to a pulsed tube cryostat and cooled down to $10\ \mathrm{K}$ before being flooded with argon. The inlet is thermally connected to the $65\ \mathrm{K}$ stage of the cryostat to freeze out water before it can reach the copper foil. The flow of noble gas is regulated by a mass flow controller to $50\ \mathrm{SCCM}$ to ensure operation in the free molecular regime and typically lasts for 20 minutes. After interrupting the argon flow the background pressure drops to $5 \cdot 10^{-7}\ \mathrm{mbar}$ reproducing the conditions in the cavity cooling experiment. Nanoparticles are then created in situ by laser desorption with an identical setup and laser parameters as before and introduced into the cryogenic matrix. After 1000 pulses and moving the focus a few times on the sample a clean silicon wafer is inserted below the target before warming up. Above the freezing point of argon at $80\ \mathrm{K}$ the matrix starts to evaporate, releasing the injected nanoparticles. They are captured on the silicon wafer and analysed by scanning electron microscopy. While the results can be considered an indication that the method works in principle, the setup has to be modified

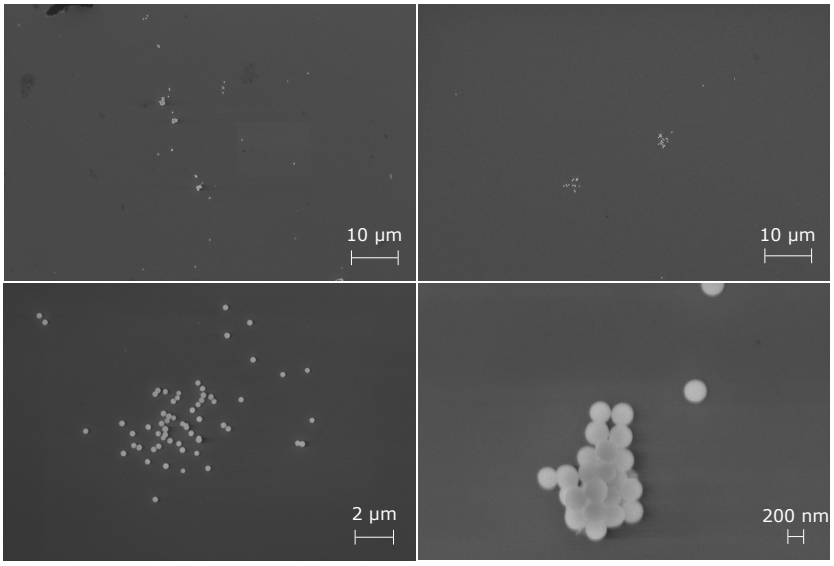

Figure 5.3: SEM images of silica nanoparticles released from a cryogenic matrix with different resolution. The clustering may occur in the matrix or during the preparation of the sample

and further characterized. In order to repeatedly deposit and launch particles, i.e. to increase the duty cycle the foil must be heated locally, e.g. by a laser or a resistive layer while being cooled. In this way the cryocooler also acts as a pump to maintain a low base pressure while particles are being launched. Optimization of the experimental parameters requires a real-time measurement of the layer thickness such as an optical interferometer. Finally, a velocity resolved nanoparticle detection as provided by a cavity itself will show if a reduction of initial kinetic energy can be achieved with this method.

5.2 Microcavities

While the currently installed microcavities have a previously unattainable high finesse they are not yet suitable for cooling. For the desired 10^7 amu nanoparticles the finesse even has to exceed 350.000. It is now limited by the imperfect

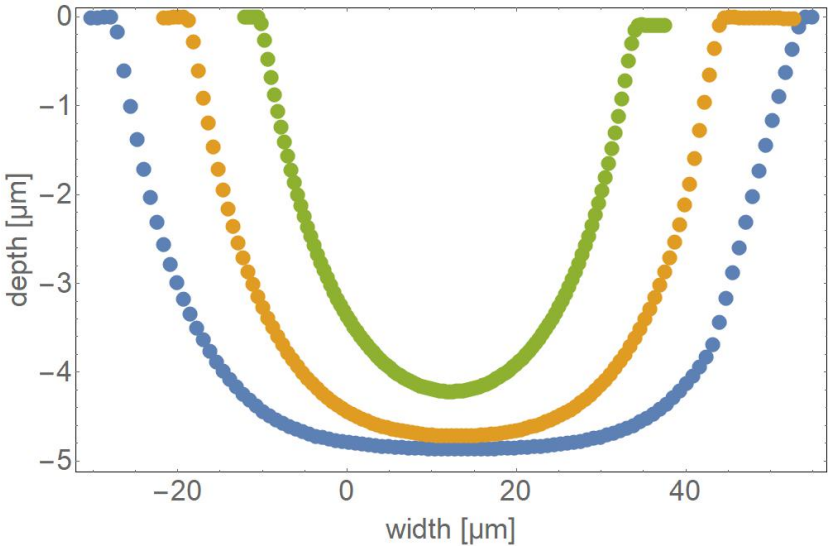

Figure 5.4: Mirror cross section of currently used microcavities from atomic force microscopy measurement. The blue curve shows the profile of $(1, 2)$ which deviates from the ideal shape. The green curve shows a different mirror on the same chip and a more spherical shape which is too small. Data were taken by G. Wachter and M. Trupke, University of Vienna.

shape of the mirrors. They deviate significantly from the ideal spherical geometry and in some cases have an almost rectangular shape. Furthermore, the etching process often penetrates too deep into the material leaving sharp edges that complicate the subsequent coating. This problem will partly be resolved in a new set of microcavities. By optimizing the etching parameters the mirror shown in green in Fig. 5.4 can be made bigger while maintaining its favorable shape. We expect a higher finesse due to the improved shape and hence the spacers can be made longer which facilitates the injection of nanoparticles. However, our results also show that in a chip-based setup like this the particle trajectory seems to be subject to considerable deflection. This issue has to be resolved if the particles are to enter an interferometer after passing the cavity.

5.3 Matter-wave interferometry

The advancement of matter-wave interferometry relies critically on the availability of suitable sources. The transition from thermal sources producing fast beams to cold, well-controlled clouds has caused a significant improvement in experiments with atoms. Atom interferometers now use carefully shaped laser light to impart momentum kicks up to $100\ \hbar\mathrm{k}$ and create large wavepaket separations [71]. The interference pattern that emerges upon recombination is very sensitive to phase shifts and can serve as a detection for gravitational fields and even tidal forces due to spacetime curvature of nearby heavy objects [72]. The sensitivity of modern atom interferometers stems from the high phase-space density and long coherence times achieved by laser cooling. Potential applications include geodesy and navigation. Many phenomena in quantum optics with massive particles and analogies to light were first observed with neutrons [73]. The de Broglie wavelength of thermal neutrons is on the order of the lattice constant in solids and their diffraction has become one of the most important tools in studying structure and dynamics. Large separations are routinely achieved in perfect single-crystal interferometers [74]. For complex molecules interferometry in the optical near-field has been established as the most viable route towards higher masses. Apart from possible applications in sensing and molecular metrology [75], composite objects such as metal clusters or nanoparticles are favourable for fundamental tests of the superposition principle. An adequate measure for the macroscopicity of a superposition state of the center-of-mass motion can be given in terms of the parameter region of a modification of the Schrödinger equation excluded by an interference measurement [76]. While Bose-Einstein condensates from millions of atoms are comparable in mass to nanoparticles, they only exclude a smaller set of parameters due to the single-particle nature of

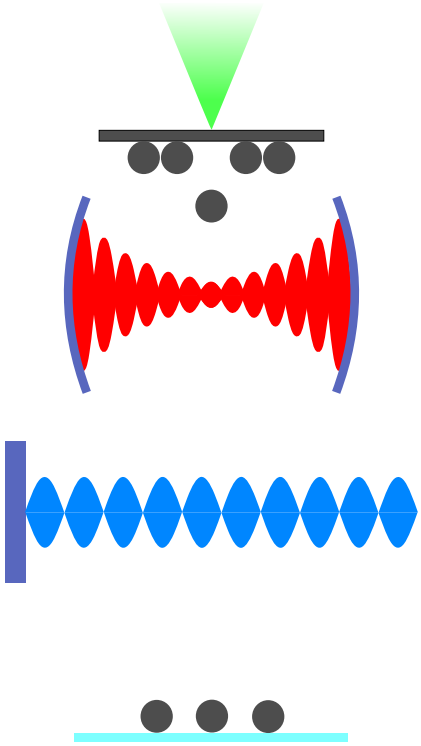

Figure 5.5: Schematic representation of a matter-wave interferometer for nanoparticles. Following cavity cooling in free flight the expanding wavepaket is diffracted at an optical grating formed by a single retroreflected laser beam or a combination of multiple gratings. The interference pattern can be imaged by collecting the particles and performing optical or electron microscopy.

their wavefunction. In Talbot interferometry a grating produces self-images imprinted onto the density of a particle beam. While state-of-the-art matter-wave interferometers use an identical grating to prepare the required transverse coherence the effect can in principle be observed with a single grating and a sufficiently coherent source. A corresponding experiment has been proposed for free-falling nanoparticles [77]. Here, silicon spheres with $m = 10^6$ amu would be captured in a dipole trap, localized by applying feedback cooling and subsequently released to be diffracted at a laser grating [78]. Mechanical gratings have a fabrication limit at a slit width of around 30 nm and a period of approximately 50 nm but would clog rapidly. Furthermore, the van der Waals interaction causes strong

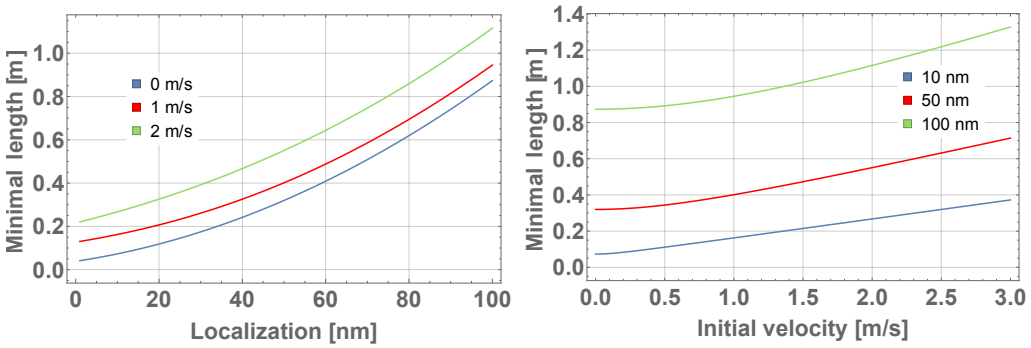

Figure 5.6: Minimal length for first order Talbot interference with $m = 10^6$ amu nanoparticles in a fountain configuration with a grating wavelength of 266 nm as a function of localization and initial velocity.

dephasing. Therefore, optical phase gratings are prefered as long as photon absorption is strongly suppressed at the given wavelength. A similar experiment can be performed using cavity cooling where the transverse velocity of the particles is reduced in transit. Microcavities naturally provide a better collimation along the optical axis but also in the other transverse dimension because of a tighter focus as compared to regular cavities. The coherence length taking into account the time evolution of momentum due to gravity is given by

$$L_c(t) = \frac{4\pi\hbar\left(vt + g\frac{t^2}{2}\right)}{\sigma_x m(v + gt)} \tag{5.3}$$

where σ_x is the size of the source, i.e. the initial localization. We require $L_c > a \cdot d$ for some $a > 1$ at the position of the grating. For a given σ_x, v_0 and a we can use (5.3) to estimate the minimal length of the interferometer for first order Talbot interference in a single grating setup. Already at $\sigma_x = 100$ nm the required distance from the source to the detector seems feasible in an earth-based experiment.

In conclusion, matter-wave optics with nanoparticles offers an intriguing platform for quantum mechanics in a largely unexplored domain. In particular, gravita-

tional phenomena [79–81] should become accessible and allow further insight not just on the nature of decoherence but also on the interplay between quantum mechanics and general relativity. While being experimentally challenging, an earth-based interferometer is still realistic. The development of optical cooling methods will be crucial step towards this goal and the presented results suggest that a first demonstration of cavity cooling in a microcavity is within reach.

Bibliography

1. De Broglie, L. Waves and quanta. *Nature* **112,** 540 (1923).

2. Davisson, C. J. & Germer, L. H. The scattering of electrons by a single crystal of nickel. *Nature* **119,** 558 –560 (1927).

3. Estermann, I. & Stern, O. Beugung von Molekularstrahlen. *Z. Physik* **61,** 95–125 (1930).

4. Halban, H. v. J. & Preiswerk, P. Preuve expérimentale de la diffraction des neutrones. *C.R. Acad. Sci.* **203,** 73 –75 (1936).

5. Arndt, M *et al.* Wave – particle duality of C_{60} molecules. *Nature* **401,** 680–682 (1999).

6. Schrödinger, E. Die gegenwärtige Situation in der Quantenmechanik. *Naturwissenschaften* **23,** 807–812 (1935).

7. Kovachy, T *et al.* Quantum superposition at the half-metre scale. *Nature* **528,** 530–533 (2015).

8. Eibenberger, S., Gerlich, S., Arndt, M., Mayor, M. & Tüxen, J. Matter-wave interference of particles selected from a molecular library with masses exceeding 10,000 amu. *Phys. Chem. Chem. Phys.* **15,** 14696–14700 (2013).

9. Bassi, A., Lochan, K., Satin, S., Singh, T. P. & Ulbricht, H. Models of wave-function collapse, underlying theories, and experimental tests. *Rev. Mod. Phys.* **85,** 471–527 (2013).

10. Diósi, L. Models for universal reduction of macroscopic quantum fluctuations. *Phys. Rev. A* **40,** 1165–1174 (1989).

11. Ghirardi, G. C., Grassi, R & Rimini, A. Continuous-Spontaneous-Reduction Model Involving Gravity. *Phys. Rev. A* **42,** 1057–1064 (1990).

12. Penrose, R. On Gravity's role in Quantum State Reduction. *Gen. Rel. Grav.* **28,** 581–600 (1996).

13. Nimmrichter, S., Hornberger, K., Haslinger, P. & Arndt, M. Testing spontaneous localization theories with matter-wave interferometry. *Phys. Rev. A* **83,** 043621 (2011).

14. Phillips, W. D. & Metcalf, H. Laser Deceleration of an Atomic Beam. *Phys. Rev. Lett.* **48,** 596–599 (1982).

15. Chu, S., Hollberg, L., Bjorkholm, J. E., Cable, A. & Ashkin, A. Three-dimensional viscous confinement and cooling of atoms by resonance radiation pressure. *Phys. Rev. Lett.* **55,** 48–51 (1985).

16. Metcalf, H. J. & van der Straten, P. Laser cooling and trapping of atoms. *J. Opt. Soc. Am. B* **20,** 887–908 (2003).

17. Dalibard, J. & Cohen-Tannoudji, C. Laser cooling below the Doppler limit by polarization gradients: simple theoretical models. *J. Opt. Soc. Am. B* **6,** 2023–2045 (1989).

18. Kasevich, M. & Chu, S. Laser cooling below a photon recoil with three-level atoms. *Phys. Rev. Lett.* **69,** 1741–1744 (1992).

19. Inguscio, M. & Fallani, L. *Atomic physics: precise measurements and ultracold matter* (Oxford University Press, 2015).

20. Bloch, I., Dalibard, J. & Zwerger, W. Many-body physics with ultracold gases. *Rev. Mod. Phys.* **80,** 885–964 (2008).

21. Bloch, I. Quantum coherence and entanglement with ultracold atoms in optical lattices. *Nature* **453,** 1016 –1022 (2008).

22. Brown, K. R., Kim, J. & Monroe, C. Co-designing a scalable quantum computer with trapped atomic ions. *npj Quantum Inf.* **2** (2016).

23. Shuman, E. S., Barry, J. F. & DeMille, D. Laser cooling of a diatomic molecule. *Nature* **467,** 820–823 (2010).

24. Kozyryev, I. *et al.* Sisyphus Laser Cooling of a Polyatomic Molecule. *Phys. Rev. Lett.* **118,** 173201 (2017).

25. Ni, K. *et al.* A High Phase-Space-Density Gas of Polar Molecules. *Science* **322,** 231–236 (2008).

26. Danzl, J. G. *et al.* An ultracold high-density sample of rovibronic ground-state molecules in an optical lattice. *Nat. Phys.* **6,** 265–270 (2010).

27. Hutzler, N. R., Lu, H.-I. & Doyle, J. M. The Buffer Gas Beam: An Intense, Cold, and Slow Source for Atoms and Molecules. *Chem. Rev.* **112,** 4803 –4827 (2012).

28. Hemmerling, B., Drayna, G. K., Chae, E., Ravi, A. & Doyle, J. M. Buffer gas loaded magneto-optical traps for Yb, Tm, Er and Ho. *New J. Phys.* **16** (2014).

29. Spaun, B. *et al.* Continuous probing of cold complex molecules with infrared frequency comb spectroscopy. *Nature* **533,** 517–520 (2016).

30. Vutha, A. C. *et al.* Search for the electric dipole moment of the electron with thorium monoxide. *J. Phys. B* **43** (2010).

31. Ashkin, A., Dziedzic, J. M., Bjorkholm, J. E. & Chu, S. Observation of a single-beam gradient force optical trap for dielectric particles. *Opt. Lett.* **11,** 288 (1986).

32. Ashkin, A & Dziedzic, J. Optical trapping and manipulation of viruses and bacteria. *Science* **235,** 1517–1520 (1987).

33. Ashkin, A., Dziedzic, J. & Yamane, T. Optical trapping and manipulation of single cells using infrared laser beams. *Nature* **330,** 769–771 (1987).

34. Li, T., Kheifets, S. & Raizen, M. G. Millikelvin cooling of an optically trapped microsphere in vacuum. *Nat. Phys.* **7,** 527–530 (2011).

35. Gieseler, J., Deutsch, B., Quidant, R. & Novotny, L. Subkelvin parametric feedback cooling of a laser-trapped nanoparticle. *Phys. Rev. Lett.* **109,** 103603 (2012).

36. Arita, Y., Mazilu, M. & Dholakia, K. Laser-induced rotation and cooling of a trapped microgyroscope in vacuum. *Nat. Commun.* **4,** 2374 (2013).

37. Bhattacharya, M. Rotational cavity optomechanics. *JOSA B* **32,** B55 (2015).

38. Hoang, T. M. *et al.* Torsional optomechanics of a levitated nonspherical nanoparticle. *Phys. Rev. Lett.* **117,** 123604 (2016).

39. Ranjit, G., Cunningham, M., Casey, K. & Geraci, A. A. Zeptonewton force sensing with nanospheres in an optical lattice. *Phys. Rev. A* **93,** 053801 (2016).

40. Rodenburg, B, Neukirch, L. P., Vamivakas, A. N. & Bhattacharya, M. Quantum model of cooling and force sensing with an optically trapped nanoparticle. *Optica* **3,** 318 (2016).

41. Geraci, A. A., Papp, S. B. & Kitching, J. Short-range force detection using optically cooled levitated microspheres. *Phys. Rev. Lett.* **105,** 101101 (2010).

42. Kuhn, S. *et al.* Full rotational control of levitated silicon nanorods. *Optica* **4,** 356 –360 (2017).

43. Stickler, B. A. *et al.* Ro-Translational Cavity Cooling of Dielectric Rods and Disks. *Phys. Rev. A* **94,** 033818 (2016).

44. Simpson, S. H., Chvátal, L. & Zemánek, P. Synchronization of colloidal rotors through angular optical binding. *Phys. Rev. A* **93,** 023842 (2016).

45. Gieseler, J. *et al.* Microscopic thermodynamics with levitated nanoparticles (Conference Presentation). *Proc. SPIE* **9922,** 992208.

46. Horak, P., Hechenblaikner, G., Gheri, K. M., Stecher, H. & Ritsch, H. Cavity-Induced Atom Cooling in the Strong Coupling Regime. *Phys. Rev. Lett.* **79,** 4974–4977 (1997).

47. Vuletić, V. & Chu, S. Laser Cooling of Atoms, Ions, or Molecules by Coherent Scattering. *Phys. Rev. Lett.* **84,** 3787–3790 (2000).

48. Maunz, P. *et al.* Cavity cooling of a single atom. *Nature* **428,** 50–52 (2004).

49. Kiesel, N. *et al.* Cavity cooling of an optically levitated submicron particle. *Proc. Natl. Acad. Sci. USA* **110,** 14180–14185 (2013).

50. Asenbaum, P., Kuhn, S., Nimmrichter, S., Sezer, U. & Arndt, M. Cavity cooling of free silicon nanoparticles in high vacuum. *Nat. Commun.* **4,** 2743 (2013).

51. Millen, J., Fonseca, P. Z. G., Mavrogordatos, T., Monteiro, T. S. & Barker, P. F. Cavity cooling a single charged levitated nanosphere. *Phys. Rev. Lett.* **114,** 123602 (2015).

52. Marquardt, F., Chen, J. P., Clerk, A. A. & Girvin, S. M. Quantum Theory of Cavity-Assisted Sideband Cooling of Mechanical Motion. *Phys. Rev. Lett.* **99,** 093902 (2007).

53. Romero-Isart, O., Juan, M. L., Quidant, R. & Cirac, J. I. Toward quantum superposition of living organisms. *New J. Phys.* **12** (2010).

54. Romero-Isart, O. *et al.* Large quantum superpositions and interference of massive nanometer-sized objects. *Phys. Rev. Lett.* **107,** 020405 (2011).

55. Haslinger, P. *et al.* A universal matter-wave interferometer with optical ionization gratings in the time domain. *Nat. Phys.* **9,** 144–148 (2013).

56. Gerlich, S. *et al.* A Kapitza-Dirac-Talbot-Lau interferometer for highly polarizable molecules. *Nat. Phys.* **3,** 711–715 (2007).

57. Kessler, T. *et al.* A sub-40 mHz laser based on a silicon single-crystal optical cavity. *Nat. Photon.* **6,** 687–692 (2012).

58. Saleh, B. E. & Teich, M. C. *Fundamentals of Photonics* (Wiley, 2007).

59. Dirac, P. *The Principles of Quantum Mechanics* (Oxford University Press, 1981).

60. Nimmrichter, S. *Macroscopic Matter-wave Interferometry* PhD thesis (2013).

61. Nimmrichter, S., Hammerer, K., Asenbaum, P., Ritsch, H. & Arndt, M. Master equation for the motion of a polarizable particle in a multimode cavity. *New J. Phys.* **12** (2010).

62. Habraken, S. J. M., Lechner, W. & Zoller, P. Resonances in dissipative optomechanics with nanoparticles: Sorting, speed rectification, and transverse cooling. *Phys. Rev. A* **87,** 1–8 (2013).

63. Kuhn, S. *et al.* Cavity-Assisted Manipulation of Freely Rotating Silicon Nanorods in High Vacuum. *Nano Lett.* **15,** 5604–5608 (2015).

64. Sezer, U. *et al.* Laser-Induced Acoustic Desorption of Natural and Functionalized Biochromophores. *Anal. Chem.* **87,** 5614–5619 (2015).

65. Asenbaum, P. *Cavity cooling of silicon nanoparticles in high-vacuum* PhD thesis (2014).

66. Potts, C. A. *et al.* Tunable open-access microcavities for on-chip cavity quantum electrodynamics. *Appl. Phys. Lett.* **108,** 041103 (2016).

67. Asenbaum, P. & Arndt, M. Cavity stabilization using the weak intrinsic birefringence of dielectric mirrors. *Opt. Lett.* **36,** 3720–3722 (2011).

68. Hunter, J. M., Lin, H & Becker, C. H. Cryogenic frozen solution matrixes for analysis of DNA by time-of-flight mass spectrometry. *Anal. Chem.* **69,** 3608–3612 (1997).

69. Sacramento, R. L., Scudeller, L. A., Lambo, R., Crivelli, P. & Cesar, C. L. Spectroscopy of lithium atoms sublimated from isolation matrix of solid Ne. *J. Chem. Phys.* **135** (2011).

70. Dhuley, R. C., Bosque, E. S. & Van Sciver, S. W. Cryodeposition of nitrogen gas on a surface cooled by helium II. *AIP Conf. Proc.* **1537,** 626–632 (2014).

71. Chiow, S.-w., Kovachy, T., Chien, H.-c. & Kasevich, M. A. 102 hk Large Area Atom Interferometers. *Phys. Rev. Lett.* **107,** 130403 (2011).

72. Asenbaum, P. *et al.* Phase Shift in an Atom Interferometer due to Space-time Curvature across its Wave Function. *Phys. Rev. Lett.* **118,** 183602 (2017).

73. Rauch, H. & Werner, S. A. *Neutron Interferometry: Lessons in Experimental Quantum Mechanics, Wave-Particle Duality, and Entanglement* (Oxford University Press, 2015).

74. Zawisky, M, Baron, M, Loidl, R & Rauch, H. Testing the world's largest monolithic perfect crystal neutron interferometer. *Nucl. Instr. Meth.* **481,** 406–413 (2002).

75. Rodewald, J. *et al.* New avenues for matter-wave-enhanced spectroscopy. *Appl. Phys. B* **123,** 3 (2016).

76. Nimmrichter, S. & Hornberger, K. Macroscopicity of mechanical quantum superposition states. *Phys. Rev. Lett.* **110,** 160403 (2013).

77. Bateman, J., Nimmrichter, S., Hornberger, K. & Ulbricht, H. Near-field interferometry of a free-falling nanoparticle from a point-like source. *Nat. Commun.* **5,** 4788 (2014).

78. Juffmann, T., Nimmrichter, S., Arndt, M., Gleiter, H. & Hornberger, K. New Prospects for de Broglie Interferometry. *Found. Phys.* **42,** 98–110 (2010).

79. Wang, C., Bingham, R. & Mendonça, T. Quantum gravitational decoherence of matter waves. *Class. Quant. Grav.* **23,** 59–65 (2006).

80. Reynaud, S., Lamine, B., Lambrecht, A., Neto, P. M. & Jaekel, M.-T. HYPER and Gravitational Decoherence. *Gen. Rel. Grav.* **36,** 2271–2288 (2004).

81. Pikovski, I., Zych, M., Costa, F. & Brukner, C. Universal decoherence due to gravitational time dilation. *Nat. Phys.* **11,** 668–672 (2017).

Appendix

Zusammenfassung

Optomechanik ist ein schnell voranschreitendes Feld mit vielversprechenden Anwendungsmöglichkeiten in Tests der fundamentalen Naturgesetze, der Thermodynamik bis hin zu sehr präzisen Messungen. Technologischer Fortschritt im Bereich der Fabrikation von Mikro- und Nanooptik ermöglicht nunmehr die Erforschung neuer Parameterregime mit diesen Systemen. Insbesondere haben sich einzelne Nanoteilchen in mikroskopischen optischen Resonatoren als möglicher Weg zum Nachweis von Quanteneigenschaften auf mesoskopischen und schließlich auch makroskopischen Skalen hervorgetan. Aufgrund ihrer Größe sind sie gut geeignet, um das Superpositionsprinzip, dem viele der eigenartigen Phänomene der Quantenmechanik entspringen, experimentell zu untersuchen. Laserkühlung in optischen Resonatoren erlaubt es, die Bewegung von Nanoteilchen durch ihre Wechselwirkung mit Licht zu verlangsamen und sie auf diese Weise für Materiewelleninterferometrie vorzubereiten. Eine Reihe neuartiger Mikroresonatoren mit hoher Güte und freiem Zugang zu diesem Zweck wurde entwickelt und in einem eigens dafür erstellten Aufbau getestet. Zudem konnte eine dispersive Wechselwirkung mit der Mode beobachtet werden und die Laserkühlung in einem Massenbereich von $10^6 - 10^9\ \mathrm{amu}$ scheint nun in unmittelbarer Reichweite.

Data analysis

Picomotor calibration

```
(*Data*)

PicomotorX = {{22100, 22400, 22930, 22540, 22500, 22460, 22200, 22260, 23080},
              {-21800, -22600, -22150, -22180, -22040, -21520, -22210, -22180, -22100},
              {22420, 23160, 22300, 22400, 22100, 22600, 22240, 22140, 22200},
              {22400, 22800, 22200, 22450, 21800, 20900, 21200, 21100, 21700},
              {-21500, -22300, -21500, -20900, -20200, -19300, -19200, -19200, 0},
              {21900, 21600, 22900, 22200, 20700, 20200, 20500, 21500, 0},
              {-21000, -22100, -20350, -19245, -19100, 0, 0, 0, 0},
              {22050, 22500, 21600, 20600, 21000, 0, 0, 0, 0},
              {-21400, -22100, -20300, -19300, -18950, -18500, -18650, 0, 0},
              {22000, 22000, 21350, 20250, 20100, 19650, 19500, 0, 0}};

PicomotorY = {{140, 500, 280, 220, 200, 220, 340, 260, 340},
              {-150, -150, -150, 88, 1, 180, -160, 920, 100},
              {240, 680, 140, 430, -50, 140, 300, 200, 320},
              {200, 300, 300, 300, 150, 200, 200, 300, 250},
              {50, -300, -100, -200, -150, -250, -200, -300, 0},
              {750, 600, 400, 250, 350, 250, 1100, 600, 0},
              {1, -250, 1800, 950, -100, 0, 0, 0, 0},
              {250, 300, 300, -350, 50, 0, 0, 0, 0},
              {-250, -350, -200, -250, -250, -250, -150, 0, 0},
              {400, 350, 300, 350, 300, 300, 300, 0, 0}};

StepSizeX = Table[N[Mean[Cases[Transpose[PicomotorX][[All, i]], Except[0]]]], {i, 1, 10}];
StepSizeY = Table[N[Total[Transpose[PicomotorY][[All, i]]]], {i, 1, 10}];

Tilt = {N[ArcTan[StepSizeY[[1]] / (StepSizeX[[1]] * 9)] / Degree],
        N[ArcTan[StepSizeY[[2]] / (StepSizeX[[2]] * 9)] / Degree],
        N[ArcTan[StepSizeY[[3]] / (StepSizeX[[3]] * 9)] / Degree],
        N[ArcTan[StepSizeY[[4]] / (StepSizeX[[4]] * 9)] / Degree],
        N[ArcTan[StepSizeY[[5]] / (StepSizeX[[5]] * 8)] / Degree],
        N[ArcTan[StepSizeY[[6]] / (StepSizeX[[6]] * 8)] / Degree],
        N[ArcTan[StepSizeY[[7]] / (StepSizeX[[7]] * 5)] / Degree],
        N[ArcTan[StepSizeY[[8]] / (StepSizeX[[8]] * 5)] / Degree],
        N[ArcTan[StepSizeY[[9]] / (StepSizeX[[9]] * 7)] / Degree],
        N[ArcTan[StepSizeY[[10]] / (StepSizeX[[10]] * 7)] / Degree]};

(*Calculate mean ste size and tilt*)
500 * 10^(-6) / Mean[Select[StepSizeX, # > 0 &]] * 10^9
500 * 10^(-6) / Mean[Select[StepSizeX, # < 0 &]] * 10^9
Mean[Abs[Tilt]][[1]]
```

Finesse

```
(*Import data*)
Files = FileNames["*.dat", NotebookDirectory[]];
DataLength = Length[Files];
SidebandFit[x_] := I0 / (1 + 4 * F^2 / Pi^2 * (x - x0)^2) + I1 / (1 + 4 * F^2 / Pi^2 * (x - (x0 - x1))^2) +
   I1 / (1 + 4 * F^2 / Pi^2 * (x - (x0 + x1))^2) + A;
ModulationFrequency = 200; (*MHz*)
fsr = 1.25;(*THz*)

(*Nonlinear fit*)
Data = ParallelTable[Import[Files[[j]]], {j, 1, DataLength}];
FinesseFit =
  ParallelTable[FindFit[Data[[i]], SidebandFit[x],
    {{x0, 0.00001}, {x1, 0.0005}, {I0, 0.1}, {I1, 0.04}, {F, 10000}, {A, 0.0001}}, x],
   {i, 1, DataLength}];

Manipulate[
 Show[
  ListLinePlot[
   Transpose[{Data[[i, All, 1]] * ModulationFrequency / Abs[FinesseFit[[i, 2, 2]]],
     Data[[i, All, 2]]}], PlotRange → All, Frame → True, Axes → False,
   FrameLabel → {"Frequency [MHz]", "Intensity [a.u.]"}, Frame → True,
   FrameTicks → {{Automatic, Automatic}, {Automatic, Automatic}},
   LabelStyle → Directive[Bold, FontSize → 14], PlotRange → {-400, 400},
   ImageSize → 500],
  Plot[SidebandFit[Abs[FinesseFit[[i, 2, 2]]] * x / ModulationFrequency] /. FinesseFit[[i]],
   {x, -400, 400}, PlotStyle → Red, PlotRange → All]],
 {i, 1, DataLength, 1}]
```

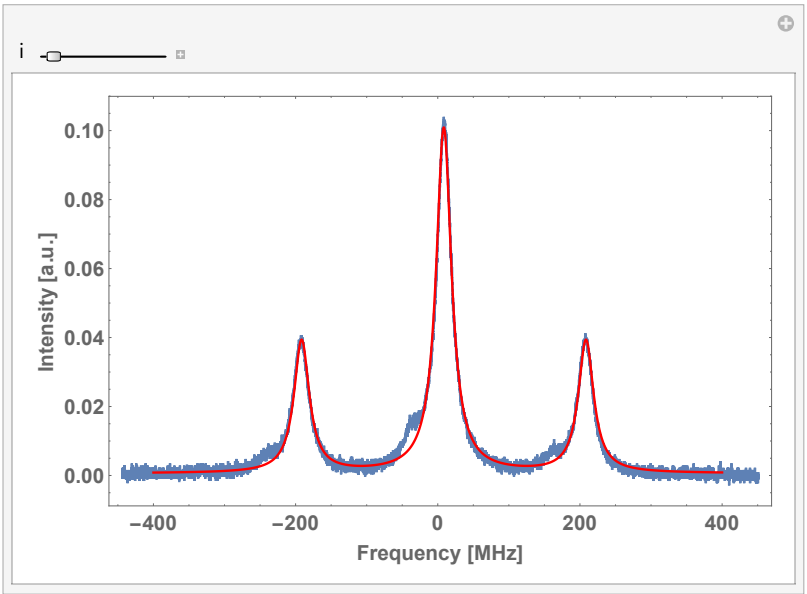

```
ClearAll[y1, y2, x];

(*Calculate linewidth*)
Linewidth =
  Table[
   {y1, y2} =
    x /. NSolve[(SidebandFit[x] /. FinesseFit[[i]]) ==
        FinesseFit[[i, 3, 2]] / 2 + FinesseFit[[i, 6, 2]], x, Reals];
   FWHM = Abs[y1 - y2] * ModulationFrequency / Abs[FinesseFit[[i, 2, 2]]]
   , {i, 1, 100}];
kappa = Mean[Linewidth]
Finesse = fsr * 10 ^ (12) / (kappa * 10 ^ 6)
Error = Finesse * (StandardDeviation[Linewidth] / kappa)
GraphicsRow[{Histogram[Linewidth, 20], ListPlot[Linewidth, GridLines → {None, {kappa}}]},
 ImageSize → Large]
filename = FileNameJoin[{NotebookDirectory[], "r1c2.wl"}];
Save[filename, Finesse]
```

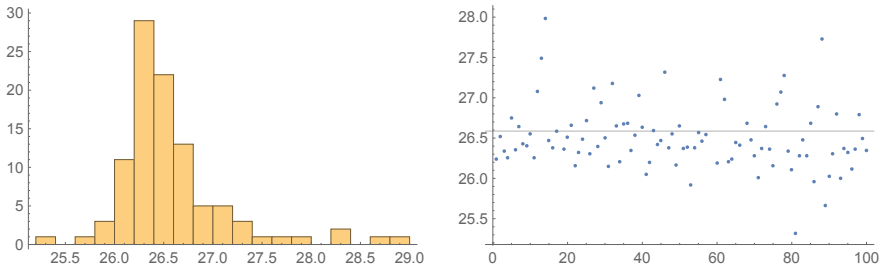

Radius of curvature

```
Clear[R, y]

(*Define constants*)
c = 299 792 458; (*m/s*)
amu = 1.66054 * 10^(-27);
e = 12.1; (*permittivity silicon*)
kappa = 26.23;(*cavity linewidth in MHz*)

(*Data*)
v1 = c / (1547.27 * 10^(-9)); (*TEM00 in Hz*)
v2 = c / (1545.91 * 10^(-9)); (*TEM01 in Hz*)
vfsr = 1.25 * 10^12;(*free spectral range in Hz*)

(*Calculate radius of curvature*)
d = c / (2 * vfsr)
R = x /. NSolve[(vfsr / Pi) * ArcCos[1 - d / x] == Abs[v1 - v2], x]

Waist[d_, R_] := (c * d / (2 * Pi * v1) * (2 * Abs[R] / d - 1)^0.5)^0.5;
W0 = Waist[d, R]

(*Coupling strength and critical radius*)
g0[r_] := 3 * Pi * v1 * (4 Pi / 3 * r^3) / (Pi * W0^2 * d / 4) * (e - 1) / (e - 2);

Rc = y /. NSolve[10^(-6) * g0[10^(-9) y] == kappa, y, Reals][[1]]
4 Pi / 3 (Rc * 10^(-9))^3 * 2200 / amu

Plot[10^(-6) * g0[10^(-9) x], {x, 0, 100}, GridLines → {{Rc}, {kappa}}, Frame → True,
 FrameLabel → {{"Coupling strength [MHz]", None},
   {"Nanoparticle radius [nm]", "Nanoparticle mass [amu]"}},
 FrameTicks → {{Automatic, Automatic},
   {Automatic, {#, NumberForm[4 Pi / 3 (# * 10^(-9))^3 * 2200 / amu, 2]} & /@
     FindDivisions[{0, 100}, 5]}}, LabelStyle → Directive[Bold, FontSize → 16],
 PlotStyle → Red, ImageSize → 500]
```

Particle detection

```
(*Import data*)
SetDirectory[NotebookDirectory[]];

Files = FileNames["*.dat", NotebookDirectory[]];
DataLength = Length[Files];

Data = ParallelTable[Import[Files[[j]]], {j, 1, DataLength}];

TimeTrace = Data[[3]];
Reflection = Import[Files[[4]]];
dt = 100;

(*Determine particle position*)
ParticlePosition = Ordering[TimeTrace[[All, 2]], -1][[1]];
T1 = TimeTrace[[ParticlePosition - dt, 1]];
T2 = TimeTrace[[ParticlePosition + dt, 1]];

Clear[a, b, c, d, W0]

W0 = 24 * 10^(-6);
Lambda = 1550 * 10^(-9);

Envelope =
  TimeSeriesWindow[
   LowpassFilter[TimeSeries[Take[TimeTrace, {ParticlePosition - dt, ParticlePosition + dt}]],
    0.03], {0.000855, 0.000859}];

(*Fit Gaussian envelope*)
Int[x_] := a * Exp[-(x - c)^2 / (2 b^2)] + d;
GaussianFit = NonlinearModelFit[Envelope, Int[x],
   {{a, 0.15}, {b, 0.000001}, {c, 0.000857}, {d, 0.12}}, x];

DataSelect = Select[TimeTrace, #[[1]] > T1 && #[[1]] < T2 &];

(*Detect intensity maxima due to transverse motion*)
Peaks = Select[DataSelect PeakDetect[DataSelect[[All, 2]], 1, Automatic, 0.13], #[[2]] > 0 &];

(*Calculate forward and transverse velocity*)
vx = W0 / (b * (2 * Log[2])^0.5 /. GaussianFit["BestFitParameters"])
vz = Lambda / Abs[Peaks[[3, 1]] - Peaks[[5, 1]]]
```